J. Fluid Mech. (2012), *vol.* 699, *pp.* 320–351. © Cambridge University Press 2012
doi:10.1017/jfm.2012.107

Coherent structures and dominant frequencies in a turbulent three-dimensional diffuser

Johan Malm†, Philipp Schlatter and Dan S. Henningson

Linné FLOW Centre, Swedish e-Science Research Centre (SeRC) and KTH Mechanics, Osquars Backe 18, SE-100 44 Stockholm, Sweden

(Received 1 June 2011; revised 17 November 2011; accepted 10 February 2012; first published online 12 April 2012)

Dominant frequencies and coherent structures are investigated in a turbulent, three-dimensional and separated diffuser flow at $Re = 10\,000$ (based on bulk velocity and inflow-duct height), where mean flow characteristics were first studied experimentally by Cherry, Elkins and Eaton (*Intl J. Heat Fluid Flow*, vol. 29, 2008, pp. 803–811) and later numerically by Ohlsson *et al.* (*J. Fluid Mech.*, vol. 650, 2010, pp. 307–318). Coherent structures are educed by proper orthogonal decomposition (POD) of the flow, which together with time probes located in the flow domain are used to extract frequency information. The present study shows that the flow contains multiple phenomena, well separated in frequency space. Dominant large-scale frequencies in a narrow band $St \equiv fh/u_b \in [0.0092, 0.014]$ (where h is the inflow-duct height and u_b is the bulk velocity), yielding time periods $T^* = Tu_b/h \in [70, 110]$, are deduced from the time signal probes in the upper separated part of the diffuser. The associated structures identified by the POD are large streaks arising from a sinusoidal oscillating motion in the diffuser. Their individual contributions to the total kinetic energy, dominated by the mean flow, are, however, small. The reason for the oscillating movement in this low-frequency range is concluded to be the confinement of the flow in this particular geometric set-up in combination with the high Reynolds number and the large separated zone on the top diffuser wall. Based on this analysis, it is shown that the bulk of the streamwise root mean square (r.m.s.) value arises due to large-scale motion, which in turn can explain the appearance of two or more peaks in the streamwise r.m.s. value. The weak secondary flow present in the inflow duct is shown to survive into the diffuser, where it experiences an imbalance with respect to the upper expanding corners, thereby giving rise to the asymmetry of the mean separated region in the diffuser.

Key words: jets, separated flows, turbulence simulation

1. Introduction

The topic of three-dimensional separation is difficult to attack, and, despite its importance in technical applications, relatively few studies have so far been conducted. Rather than predicting three-dimensional separation, some investigations focus merely on interpreting the nature of it from an already given flow field, further discussed in the review by Délery (2001). Other authors have tried to predict the separation by means of turbulence closure models, among them the periodic hill configuration

† Email address for correspondence: johan@mech.kth.se

https://doi.org/10.1017/jfm.2012.107 Published online by Cambridge University Press

investigated by Wang, Jang & Leschziner (2004). These authors concluded that, even though using an anisotropy-resolving closure on the simplest possible case involving separation in three dimensions, the model misses important mechanisms responsible, for example, for multiple-vortex structures in the wake. Even though engineering flows are *practically always fully three-dimensional*, most common turbulence closures fail to predict three-dimensional separation correctly. In order to accelerate the development of such models, the physical mechanisms involved in this type of separation need to be well understood. A first step in this direction was taken by Cherry, Elkins & Eaton (2008), who experimentally investigated the turbulent flow in a three-dimensional diffuser. Their idea was to create a truly three-dimensional flow case with well-defined boundary conditions in order to simplify the set-up for numerical simulations. The case has turned out to be an important test case for Reynolds-averaged Navier–Stokes (RANS) models and hybrid Reynolds-averaged Navier–Stokes/large-eddy simulation (RANS–LES) models as well as, to some extent, for validation of sub-grid scale (SGS) models (Jakirlić *et al.* 2010*b*). More specifically, Jakirlić *et al.* (2010*a*) showed promising results employing a hybrid RANS–LES scheme, whereas Schneider, von Terzi & Rodi (2009) obtained very good results using LES. The major improvement of the results using an eddy-resolving technique compared to steady RANS proves the difficulties involved in modelling such a complex, but yet realistic, flow.

Although a valuable reference for some of the mean flow quantities, the experimental compilation by Cherry *et al.* (2008) gives little insight into the presumably complex flow dynamics present in the diffuser, as time-resolved information is lacking. In an attempt to enhance the understanding of this flow, a first direct numerical simulation (DNS) was performed by Ohlsson *et al.* (2010). (Note: owing to a change of name, 'J. Ohlsson' and 'J. Malm' are one and the same person.) The good agreement between the experimental data and the numerical simulation was established, thereby founding the validity of the numerical model as a whole. As a next step, the rich data base – including not only turbulence statistics but also temporal information – can now be accessed with high fidelity. In order to obtain converged statistics, long-time integration was required. This is due not only to the lack of statistically homogeneous directions and the possibility of averaging over these, but also to the long periods associated with the unsteadiness of the flow. A re-examination of the data showed that this unsteadiness contains regularities: quasi-periodic and coherent motions, which motivated a further analysis.

One question of particular interest in flow analysis is whether there are periodic or quasi-periodic motions with specific frequencies present in the flow. Practical reasons in engineering applications may be that these motions lead to unwanted vibrations, fatigue and possibly premature breakage. If heat transfer is an issue, oscillations in the flow may lead to an uneven heat distribution, with decreased heat transfer as an effect. Separated flows, both laminar and turbulent, are characterized by large velocity fluctuations and chaotic and irregular unsteadiness. However, flows in which the separation is induced by an abrupt change in the geometry (i.e. geometry-induced separation) often show the tendency of quasi-periodic motion. A well-studied example of this kind is the turbulent flow over a backward-facing step, where dominant frequencies have been reported in numerous studies. For instance, in a DNS, Le, Moin & Kim (1997) reported a periodic behaviour of the free shear layer with Strouhal number of $St = fh/U_0 \approx 0.06$, U_0 being the free stream velocity and h the step height. A low-frequency 'flapping' motion was also observed by Eaton & Johnston (1980) in an experimental set-up of the backward-facing step. In an LES, Friedrich & Arnal (1990) noticed an oscillation of the free shear layer, which in turn caused the location of the reattachment point to oscillate back and forth. Low-frequency periodic shedding has also been observed in other configurations involving geometry-induced separation.

https://doi.org/10.1017/jfm.2012.107 Published online by Cambridge University Press

Kiya & Sasaki (1985) found periodic large-scale unsteadiness with some particular frequencies in the turbulent separation bubble formed at the leading edge of a blunt flat plate with right-angled corners.

Considering the experimental and numerical work performed on pressure-induced separated flows, where the separation is induced not by the geometry but rather by the action of the adverse pressure gradient, to our knowledge no such dominant frequencies have been reported in the literature. Often the contrary is observed: the point of separation and reattachment varies in time and space, with no particular periodicity. Accordingly, in the DNS of a pressure-induced separated turbulent boundary layer, Na & Moin (1998) noted that the shedding of large structures in the separated region is not a periodic process, but that there exists a characteristic Strouhal number $St = f\delta^*/U_0$ of the most energetic structures, which ranges between 0.0025 and 0.01, with δ^* being the displacement thickness of the incoming flow and U_0 the free stream velocity. Similar conclusions have been deduced in turbulent diffuser flows with smooth rounded corners at the diffuser throat, thus belonging to the same class of pressure-induced separated flows. This was reported to be the case in the LES of the asymmetric diffuser with 10° opening angle by Kaltenbach *et al.* (1999), with a two-dimensional geometry. They found that the separation in the rear part of the expansion is a low-frequency unsteady process involving large scales of motion, but that the unsteadiness is broadband and cannot be characterized through a single frequency. Similar findings are reported by Herbst, Schlatter & Henningson (2007), who for a similar Reynolds number decreased the opening angle to 8.5°. However, the incoming channel flow was observed to penetrate in a 'jet-like' manner into the expanding diffuser section in this reference. Likewise, in the experimental set-up of the latter case, Törnblom, Lindgren & Johansson (2009) did see a 'jet-like' high-velocity region emanating from the inlet channel, but no temporal information on the properties of this jet in particular, or the separation bubble in general, were provided, since no dominant frequencies could be detected (A. V. Johansson, private communication).

From the above discussion, it appears that pressure-induced separated flows contain to a lesser degree quasi-periodic motions. However, up till now we have considered flows without any type of confinement in the spanwise direction. If some sort of additional confinement is added to the flow, e.g. solid walls in the spanwise direction, the dynamics will inevitably change. This has previously been shown by several authors, including Villermaux & Hopfinger (1994), Maurel *et al.* (1996) and Lawson & Davidson (2001), here briefly summarized. Lawson & Davidson (2001) investigated the oscillatory behaviour of a confined jet in a rectangular cavity and reported that low-Strouhal-number oscillatory jets ($St \ll 1$, where St is based on the nozzle diameter) may occur when the confinement is such that the jet is bounded by one or two recirculation zones, created due to the close presence of the walls. These zones can, under certain circumstances, create a feedback mechanism that couples back to the jet nozzle, thereby resulting in self-sustained oscillations. They note that, by removing the recirculation zones, the feedback loop is broken and the regular jet oscillation will not occur. On the contrary, oscillations with $St \sim 1$ relate to the inherent instability of the jet shear layer and can thus be present also without the confinement. They found the low-frequency oscillation of the jet to be independent of Re, and that the relevant parameter was the width-to-length ratio of the cavity. A reduction of this ratio would lead to an increase in St until the width coincided with the nozzle diameter and the jet would cease to oscillate. However, a too large increase of this ratio would not allow the recirculation zones to form and thus no oscillations of the jet were observed. The implication is that there exists a peak of the amplitude of the oscillation for some width-to-length ratio, e.g. a given shape of the confinement. Lawson & Davidson (2001) found that this ratio corresponded to the same ratio giving the highest

https://doi.org/10.1017/jfm.2012.107 Published online by Cambridge University Press

cross-flow disturbance velocities at the nozzle of the jet, caused by the recirculation. The fact that the width of the cavity is one of the most important parameters governing the presence of self-sustained oscillations was earlier confirmed by Maurel *et al.* (1996), who also argued that the nozzle width imposes the selected wavelengths within the values allowed by the boundary conditions imposed by the length of the domain. Another study on confined jets in a rectangular cavity at different Re by Villermaux & Hopfinger (1994) resulted in similar conclusions. In particular, they concluded that a free jet does not display low-frequency oscillations and that these oscillations are due to the confinement. They further state that the role of the confinement is to establish recirculation zones adjacent to the jet, which then convect high-amplitude perturbations upstream. These perturbations will interact with the shear instability of the jet after a certain time lag, given by the upstream convection velocity in the recirculation zone. They report that, for sufficiently high Re, the mean reattachment length, and likewise St, becomes independent of Re, and is found to be $St \sim 0.01$ (based on the nozzle diameter). For asymmetric configurations, it was found that the largest confinement dimension will dominate the flow.

The present flow case is both relevant and realistic from an engineering point of view, since it combines many complex phenomena that are not fully understood even on their own but nevertheless are exclusively present in most engineering flows: turbulent separation and three-dimensionality of the mean flow in conjunction with confinement. The aim of this paper is to provide an improved physical understanding of this flow by describing the observed dynamics, which up till now has not been described in detail. An extensive investigation of the oscillatory behaviour is carried out. The search for dominant frequencies is undertaken both by performing spectral analysis on a set of time signal probes and by proper orthogonal decomposition (POD) of the flow. The latter is also used to identify coherent structures associated with the dominant frequencies. The significance of the large-scale structures on the mean fluctuations of the flow is demonstrated by constructing a low-dimensional model of the flow based on the first few energetic POD modes. In Ohlsson *et al.* (2010), a slight discrepancy was found between the present DNS data and the experimental data of Cherry *et al.* (2008) regarding a pronounced vortex (referred to as 'bump') in the mean separated region. This finding gave a first indication that the reasons for and the characteristics of the separation might be more complex than expected. Here, this finding is more rigorously confirmed.

The paper is organized as follows. Section 2 briefly discusses the numerical method and the simulation set-up. In § 3.1, the evolution of the secondary flow in the diffuser together with instantaneous separations are analysed, whereas § 3.2 is devoted to the observed large-scale dynamics seen in the present DNS, investigated by means of time signal probes. Section 4 addresses the decomposition of the flow into POD modes as well as the low-dimensional reconstruction of the flow using only a few energetic modes. In particular, aspects of the global root mean square (r.m.s.) distribution are addressed via POD. Finally, in § 5, the main conclusions of the present study are given.

2. Numerical method and simulation set-up

The three-dimensional, unsteady and incompressible Navier–Stokes equations are solved using a Legendre polynomial-based spectral-element method, implemented in the code `nek5000`, developed and maintained by Fischer, Lottes & Kerkemeier (2008). For a detailed description of the spatial discretization and time integration, the reader is referred to Fischer (1997) and Tufo & Fischer (2001), whereas the main steps are outlined in Ohlsson *et al.* (2010). The computational domain, shown in figure 1, is set up in close agreement with the diffuser geometry employed in the experiment and

https://doi.org/10.1017/jfm.2012.107 Published online by Cambridge University Press

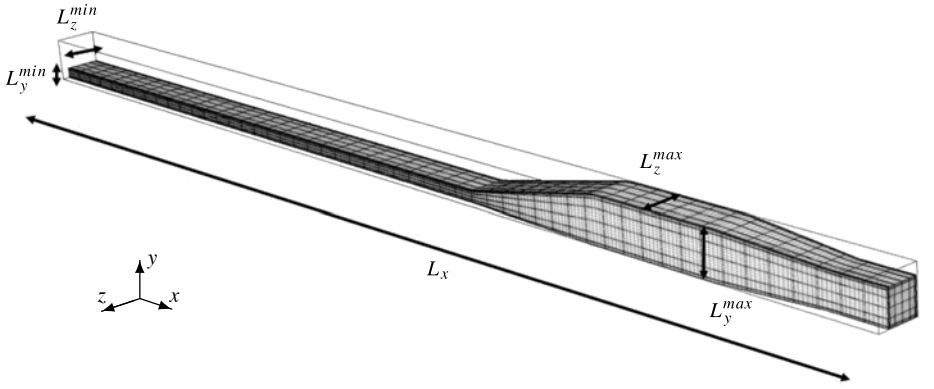


FIGURE 1. Computational grid of one of the diffuser geometries ('diffuser 1') in Cherry *et al.* (2008), showing the development region, diffuser expansion, converging section and outlet.

consists of the inflow development duct with a length of almost 63 duct heights, h (starting at the non-dimensional coordinate, $x = -62.9$), the diffuser expansion located at $x = 0$, the straight section and finally the converging section upstream of the outlet. In the following, by 'diffuser' we mean the region between $x = 0$ and $x = 15$. The three-dimensionality arises from the asymmetry of the geometrical configuration: whereas two of the walls are straight, the other two walls are deflected 11.3° in the y direction and 2.56° in the z direction (compare with the Cartesian box in figure 1). The corners resulting from the diffuser expansion are smoothly rounded with a radius of 6.0 in accordance with the experimental set-up. The maximum dimensions are $L_x = 105.4h$, $L_y = [h, 4h]$ and $L_z = [3.33h, 4h]$. The fixed mass flux in the simulation enables the Reynolds number based on bulk velocity and inflow-duct height to be kept exactly at $Re = 10\,000$, which matches the value reported in the experiment by Cherry *et al.* (2008). The resolution of approximately 220 million grid points is obtained by a total of 127 750 local tensor product domains (elements) with a polynomial order of 11, respectively, resulting in $\Delta z^+_{max} \approx 11.6$, $\Delta y^+_{max} \approx 13.2$ and $\Delta x^+_{max} \approx 19.5$ in the duct centre and the first grid point off the wall being located at $z^+ \approx 0.074$ and $y^+ \approx 0.37$, respectively. This resolution was carefully verified in Ohlsson *et al.* (2010) to yield accurate results compared to the experimental findings of Cherry *et al.* (2008). In the inflow duct, laminar flow undergoes natural transition by the use of an unsteady and random trip force with a prescribed length and time scale, successfully employed, for example, in the boundary layer simulation by Schlatter *et al.* (2009). First of all, this avoids the use of artificial turbulence where *ad hoc* parameters specifying the synthetic turbulence have to be set at the inflow plane and tuned in order to provide correct turbulent statistics further downstream. It also eliminates the spurious frequencies that have been observed in pressure-induced separated flow in conjunction with inflow recycling methods, discussed by Herbst *et al.* (2007) for the asymmetric diffuser flow. These are typically low frequencies correlated to the frequency whereby the inflow planes are fed at the inlet, also pointed out by Lygren & Andersson (1999) and Spille-Kohoff & Kaltenbach (2001), for example, and may not be noticeable in flows with favourable or zero pressure gradient. In flows subject to an adverse pressure gradient exhibiting pressure-induced separation, however, a certain periodicity of the inflow signal can potentially trigger unsteady behaviour of the detachment point of a separation bubble, also observed by Adams (2000). In Ohlsson *et al.* (2010), it was demonstrated that the trip forcing mentioned above yields a fully developed flow well before the diffuser opening. Secondly, incorporating the laminar–turbulent

https://doi.org/10.1017/jfm.2012.107 Published online by Cambridge University Press

Time range (tu_b/h)	Purpose	Discussion
0–202	Start-up	—
202–636	Statistics	Ohlsson *et al.* (2010)
384–842	Time probe data	Current
448–840	Snapshots	Current
636–840	Additional statistics	Current

TABLE 1. Overview of the time range pertaining to the present simulation.

transition in the same box further strengthens the similarities between simulation and experiments, since the flow in the experimental set-up indeed undergoes transition. Finally, a 'sponge region' is added at the end of the contraction in order to smoothly damp out turbulent fluctuations, thereby eliminating spurious pressure waves back into the domain. It is followed by a homogeneous Neumann condition for the velocities at the outflow boundary.

The simulation was performed on the Blue Gene/P at the Argonne Leadership Computing Facility (ALCF), Argonne National Laboratory (32 768 cores and a total of ∼10 million core hours), on the 'Ekman' cluster (2048 cores and a total of ∼6.0 million core hours) and on the Cray XE6 at PDC, Stockholm (32 768 cores and a total of ∼0.33 million core hours). Approximately 13 flow-through times, $tu_b/L = 13$, based on bulk velocity, u_b, and diffuser length, $L = 15h$, were spent on the start-up phase in order to let the flow settle to an equilibrium state. Then, turbulent statistics for the mean flow results in Ohlsson *et al.* (2010) were collected over approximately $tu_b/L = 29$ additional flow-through times. During part of this time instantaneous snapshots were saved and time probe data were recorded. For the present work, the simulation has been extended with additionally $tu_b/L \approx 13$ flow-through times to ensure convergence of the mean flow results and to capture the relevant dynamics in the instantaneous flow. This additional averaging time was observed to have a minute influence on the quantities already shown in Ohlsson *et al.* (2010). An overview of the various parts of the simulation is given in table 1. Already in Ohlsson *et al.* (2010) the flow was observed to be challenging: the three-dimensional configuration in combination with the large separated zones made the flow under investigation very non-stationary, which, together with the lack of spatially homogeneous directions, called for long-time integration in order to obtain converged statistics and to collect all possible time scales in the flow.

3. Analysis of averaged and instantaneous flow features

3.1. *Mean flow features*

In order to give a comprehensive picture of the flow, three-dimensional visualizations of the time-averaged streamwise velocity component $\langle u \rangle = U$ and the streamwise root mean square (r.m.s.) value, u_{rms}/u_b, are shown in figures 2(*a*) and 2(*b*), respectively. Here, $\langle \cdot \rangle$ denotes an average over the (only) homogeneous direction time. Two-dimensional visualizations (i.e. cross-flow plots) have already been given in Ohlsson *et al.* (2010), where the emphasis was on the mean flow data and the comparison to the experiment by Cherry *et al.* (2008) and Cherry, Elkins & Eaton (2009). An isosurface of nearly zero streamwise velocity ($U/u_b = 10^{-5}$) is shown in order to demonstrate the extent of the separated flow while excluding the no-slip boundaries. The dotted black line drawn at the wall indicates zero streamwise shear stress,

https://doi.org/10.1017/jfm.2012.107 Published online by Cambridge University Press

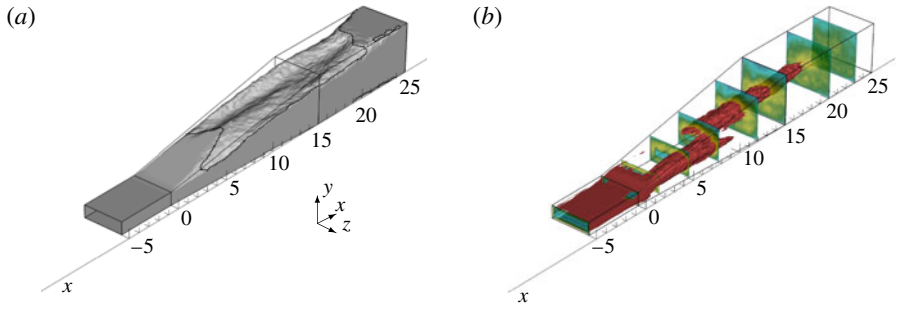


FIGURE 2. (*a*) Isosurface of (nearly) zero mean streamwise velocity ($U/u_b = 10^{-5}$). The dotted black line indicates zero streamwise shear stress, $\nabla U \cdot \boldsymbol{e_x}|_{wall} = \boldsymbol{0}$. (*b*) Isosurfaces (red) of the streamwise velocity fluctuation level $u_{rms}/u_b = 0.155$, with cross-flow planes ($x = -5,\ 0,\ 2,\ 5,\ 8,\ 12,\ 15.5,\ 20,\ 23$) showing u_{rms}/u_b with colours ranging from 0 (blue) to 0.25 (red).

i.e. $\nabla U \cdot \boldsymbol{e_x}|_{wall} = \boldsymbol{0}$, which here, as well as in Cherry *et al.* (2008), defines the extent of the separation bubble. We note that the mean separated region is large: it covers approximately half the streamwise length, the entire spanwise length (in z) and the upper quarter of the diffuser. In addition, it continues well into the straight section. As a consequence, the dynamics of the flow is expected to be largely affected by the separation, with shear layers interacting with the incoming turbulence, thereby causing a complex flow with a high degree of unsteadiness. Further, we can observe that, shortly after entering the diffuser, the flow separates in the upper right corner due to the asymmetric geometrical configuration, as was also observed in Ohlsson *et al.* (2010) and in agreement with the findings of Cherry *et al.* (2008). As we proceed downstream, the separated zone can be seen to broaden and move more towards the top expanding wall, which has the largest opening angle. Simultaneously, the flow separates to the left around $x = 6$, and this is where the so-called 'bump' initially appears, first discussed in Ohlsson *et al.* (2010). The name originated from the particular shape of the zero streamwise velocity contour in a cross-flow plane. In three dimensions, this structure (i.e. the 'bump') takes the form of a long and relatively deep 'valley', visible to the left in figure 2(*a*). Together with the separated region to the right, this results in two valleys on either side of a 'ridge', a feature that is most prominent between $x = 8$ and $x = 12$, but nevertheless dominates the shape of the separation bubble for the rest of its streamwise extent. The shape of the zero velocity surface, including the feature just mentioned, and the dotted line are in good agreement with LES of the same flow by Schneider *et al.* (2009), where a similar three-dimensional visualization is given. The major difference is that therein the first sign of separation appears on the top expanding wall just after the diffuser opening, across the entire spanwise extent of the diffuser and localized to approximately $2h$ in the streamwise direction. However, this finding is supported neither by our DNS nor by the experimental data set, but, as we shall see later in this section, instantaneous backflow is present in this region. As also evident from the streamwise fluctuations in figure 2(*b*), the flow changes drastically from an attached turbulent flow in the duct, where the bulk of the fluctuations are present close to the wall, to the separated flow in the diffuser, where the highest fluctuations are found around the centre of the domain. As noted in Cherry *et al.* (2008) and Ohlsson *et al.* (2010), when the flow has entered the diffuser, the peak u_{rms} is found in the shear layer bounding the separated zone in

https://doi.org/10.1017/jfm.2012.107 Published online by Cambridge University Press

the upper right corner. This is also where the highest overall fluctuations occur in the flow. For the particular isosurface visualized in figure 2(*b*), there is a 'double peak' appearing around $x = 8$. For lower levels of u_{rms}, this double peak emerges further downstream. The reasons for this behaviour have up until now not been addressed in any study of this flow. Here, however, this peculiar phenomenon will be further investigated and we will see that it is connected to the large-scale motions found in the diffuser.

The present flow case consists of turbulent flow in a rectangular duct, which eventually separates in the diffuser. Hence, secondary flow of the *second kind* is present due to cross-flow gradients in the Reynolds stresses (see e.g. Piquet 1999). An indication that this flow has an effect on the separation behaviour is given by the several RANS predictions documented in Jakirlić *et al.* (2010*b*). There, it was observed that most eddy viscosity models, which assume isotropic conditions and hence no secondary flow in the duct, would fail to predict the separation correctly. On the other hand, Reynolds stress models, which were able to compute the secondary flow in the duct, were in general much closer in getting a correct separation behaviour. The finding of the 'bump' discussed earlier initiated a further study on the reasons for this particular phenomenon. It was conjectured that, although very weak in magnitude, the corner vortices induced by the secondary flow in the inflow duct persist into the diffuser (Ohlsson *et al.* 2010). There, they give rise to a dominant low-speed streak, due to a similar mechanism to the so-called 'lift-up effect' in transitional shear flows (Landahl 1980), which in turn has a large influence on the separation behaviour. To further confirm these conjectures, we track here the secondary flow from the inflow duct into the diffuser by means of streamwise vorticity computed from the mean flow field, i.e. $\langle\omega_x\rangle = \partial\langle v\rangle/\partial z - \partial\langle w\rangle/\partial y$. Owing to the slow variation of mean quantities in the streamwise direction, the vorticity (and all other quantities, to be consistent) are averaged over a distance h in x. Moreover, a smoothing in the yz plane is performed by applying a mean filter over a rectangle of size two-by-two points, which basically replaces point i by the mean of the rectangle centred on i. A three-dimensional visualization of the mean streamwise vorticity is given in figure 3. Here, isosurfaces of positive vorticity are shown to indicate the corner vortex to the upper left, whereas isosurfaces of negative vorticity (of the same magnitude) show the evolution of the right vortex. Cross-flow planes with mean streamwise velocity are included, with thin black lines indicating the zero velocity contour. First of all, it is evident that the mean secondary flow continues from the duct into the diffuser. Secondly, one can observe that the right vortex is diffused rather quickly and is therefore less coherent than its left counterpart. (The definition of left and right according to figure 3.) As discussed above, when entering the diffuser, the flow separates first in the upper right corner. As an effect of the separated flow, the turbulence intensity increases (values of u_{rms}/u_b reaching 25 % were observed by Cherry *et al.* (2008) in the shear layer bounding the separation bubble). The increased turbulent activity enhances the turbulent diffusion in this region and, accordingly, the secondary flow is weakened – in particular, the negative vorticity. This is further quantified in figure 4, where a cross-flow plane at $x = 12$ is selected. The appearance of the 'bump' can now be clarified by noting the imbalance between the positive vorticity to the left and the negative vorticity to the right in figure 4(*a*). Thus, the magnitude of the vorticity to the left is greater than the magnitude of the vorticity to the right, quantified in figure 4(*b*), where the vorticity along y in the cross-flow plane at $x = 12$ is shown. Here, $z = 0.368$ and $z = 3.73$ denote the spanwise coordinates where the maximum magnitudes of positive vorticity in the upper left and negative vorticity in the upper right corners are found,

https://doi.org/10.1017/jfm.2012.107 Published online by Cambridge University Press

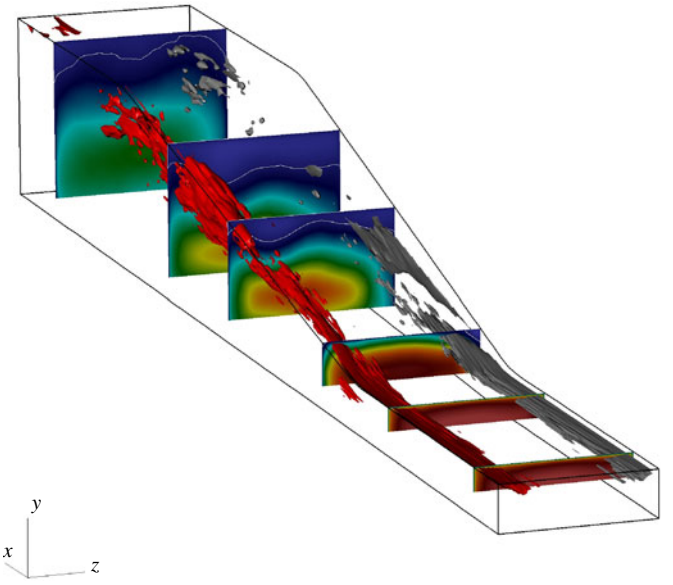


FIGURE 3. Isosurfaces of mean streamwise vorticity $\langle\omega_x\rangle = 0.15$ (red) and $\langle\omega_x\rangle = -0.15$ (dark grey), showing the evolution of the upper left and right corner vortices, respectively. Cross-flow planes of mean streamwise velocity are shown at $x = -7,\ -2,\ 2,\ 8,\ 12,\ 20$ ranging from -0.1 (blue) to 1.2 (red). Thin white lines indicate zero streamwise velocity contour.

respectively. The primary vortices responsible for the cross-flow in the vicinity of the zero streamwise velocity contour are of the main focus here, and hence the boundaries, where the vorticity locally can be very high, are excluded. From figure 4(*b*), it is evident that the left vortex is stronger (almost by a factor of two) than the one to the right. This is thought to be the basic mechanism to create and maintain the observed asymmetry in the zero streamwise velocity contour.

To conclude these considerations, owing to the choice of delivering the inflow through a duct, there is a secondary flow inherent to the mean flow. This flow has been observed to persist into the diffuser. Evaluation of the magnitude of the local vorticity shows that the left vortex is twice as strong as its right counterpart, which creates an asymmetry in the zero velocity contour. Here it should be pointed out that, owing to the asymmetry of the geometrical set-up, there is no reason to expect that the separated zone on the top expanding wall should be symmetric with respect to the z axis. Finally, it should be noted that this weak secondary flow (a few per cent of the bulk flow) that originates from the inflow duct appears in the mean. Superimposed on this flow there is momentarily a stronger cross-flow caused by the large-scale oscillation in the diffuser, to be discussed in the next section. (There is also an in-plane flow caused by the expansion, but it does not, however, contain vortices.)

The mean flow shown in figure 2 only provides information about the mean separation. Sometimes, however, it can be useful to know to what extent instantaneous separation occurs in the flow. Aiming at providing a fuller picture of this flow, we end this section by investigating the fraction of time that the flow moves in the positive streamwise direction. Traditionally, this fraction is denoted by γ (after Simpson 1981), and amounts to the following special cases: $\gamma = 1$, never backflow; and $\gamma = 0$, always backflow. In the classical review on separated flows by Simpson (1989), a few

https://doi.org/10.1017/jfm.2012.107 Published online by Cambridge University Press

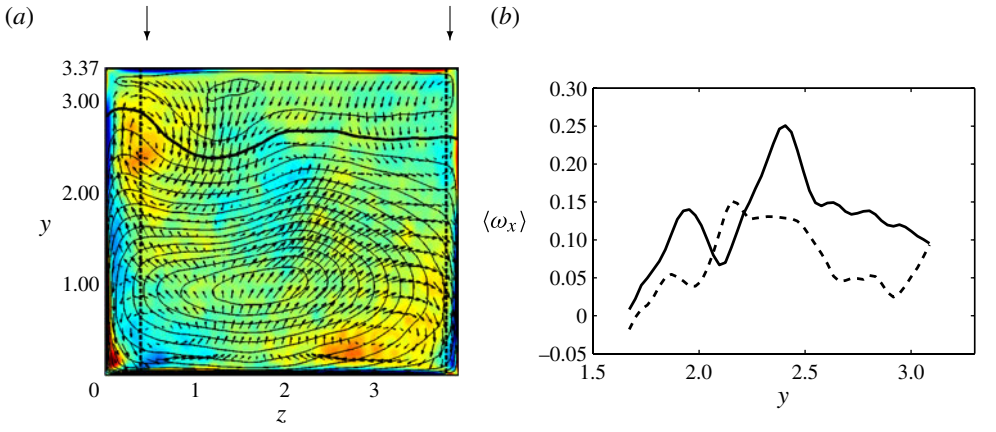


FIGURE 4. (*a*) Cross-flow plane of mean streamwise vorticity $\langle\omega_x\rangle$, $12h$ downstream of the diffuser throat, ranging from -0.5 (blue) to 0.5 (red). Contour lines of mean streamwise velocity, spaced $0.05u_b$ apart, as well as velocity vectors of mean cross-flow velocities, are superimposed. Thick black lines correspond to the zero mean streamwise velocity contour. (*b*) Plot of $\langle\omega_x\rangle$ at $z_1 = 0.368$ (——) and $-\langle\omega_x\rangle$ at $z_2 = 3.73$ (– – – –) along y in the cross-flow plane in panel (*a*) across the two primary vortex centres responsible for the maximum magnitude in the upper left and right corners, respectively. Black arrows above panel (*a*) indicate z_1 and z_2.

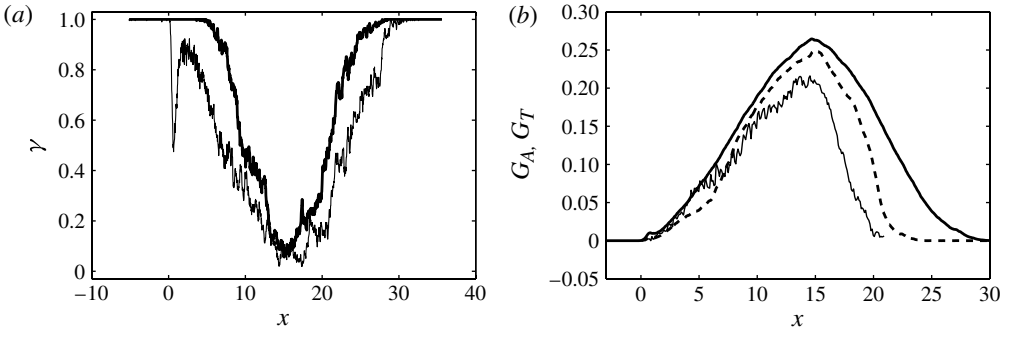


FIGURE 5. (*a*) Backflow ratio $\gamma(x)$ in y coordinates corresponding to the upper history points in figure 8 (thick curve) and in the first y point off the top expanding wall (thin curve), both taken in a spanwise midplane. (*b*) Fraction of cross-sectional area separated, $G_A(x)$ (experimental data of Cherry *et al.* (2008), thin full curve; present DNS data, dashed curve), together with the 'temporal backflow ratio', $G_T(x)$ (thick full curve).

intermediate cases are discussed in order to broaden the view on turbulent separated flows. More specifically, $\gamma = 0.99$ is the so-called *incipient detachment* (ID), where backflow occurs 1 % of the time; $\gamma = 0.80$ is the *intermittent transitory detachment* (ITD); and $\gamma = 0.50$ is the *transitory detachment* (TD). In the present case, a number of snapshots spanning a total time of $\Delta t u_b/h = 392$ were used. In figure 5(*a*), γ is computed at all x locations between $x = -5.15$ and $x = 35.6$. The y and z positions for the thick black line correspond to the upper history points in figure 8 (i.e. at the same grid point from the wall and at a spanwise mid-position). We observe

https://doi.org/10.1017/jfm.2012.107 Published online by Cambridge University Press

that backflow is never present ($\gamma = 1$) until $x \approx 4$. Then, there is a rapid increase of backflow until $x \approx 15$, when the flow is in the positive x direction only 10 % of the time, i.e. directed backwards 90 % of the time. After this point, there is an almost symmetric recovery until $x \approx 28$, after which the flow is seen to be attached again. The thin black line is computed in a spanwise mid-position and in the first y point off the top expanding wall. This is equivalent to the linear extrapolation of the corresponding fraction of positive and negative streamwise shear stress at the wall. Incipient detachment occurs already at a few places $x \in [-5, 0]$ in the turbulent duct. Then, at the location of the diffuser opening ($x = 0$), γ rapidly drops down to 0.8 ($x = 0.4$) and then further decreases to 0.5 ($x = 0.58$), after which it quickly recovers to 0.9. This behaviour approximately follows the development of the skin friction coefficient in pressure-induced separated flows, discussed by, for example, Kaltenbach *et al.* (1999) and Herbst *et al.* (2007). Since three-dimensional velocity fields were used to compute $\gamma(x)$, we are by no means restricted to the particular subset shown in figure 5(*a*). Thus, instead of choosing one specific trajectory through the data set, we could at each streamwise location integrate γ over a cross-flow plane, in order to get a more robust measure of the development of the backflow through the diffuser. More specifically, we compute the following integral in each plane:

$$G(x) = \frac{1}{A(x)} \iint_{A(x)} \gamma(x, y, z)\, \mathrm{d}x\, \mathrm{d}y. \tag{3.1}$$

The function $G(x)$ has a shape similar to $\gamma(x)$ (thick black) shown in figure 5(*a*). To be able to compare this measure to the fraction of cross-sectional area separated, provided in Cherry *et al.* (2008), here called $G_A(x)$, we will define a new quantity based on $G(x)$ called 'temporal backflow ratio': $G_T(x) = 1 - G(x)$. In figure 5(*b*), these two integral quantities are compared, with $G_A(x)$ based on the experimental data included as a reference. First of all, the comparison between $G_A(x)$ in the DNS and the experiment agree reasonably well, especially in most of the diffuser region ($x = 0$–10). Note also that the point of separation is identical. At the end of the diffuser and in the following straight section, the experiment shows somewhat less separated flow compared to the DNS, with the peak separated flow ($x = 15$) being $\sim$10 % less in the experiments. The reattachment point in the experiment is located approximately at $x = 22$, whereas the DNS reports $x = 24$. Now, comparing $G_T(x)$ and $G_A(x)$ based on the DNS, we notice that the correspondence is close early on in the diffuser. Both peaks occur at the same streamwise location ($x = 15$), but with G_T being approximately 10 % larger. In the straight section, G_T generally attains higher values. In particular, when G_A is zero ($x = 20$), G_T is non-zero for approximately $10h$ more. While this is not surprising, since indeed the contribution to the former quantity is present even for small backflow ratios, it gives important information about the dynamics. Thus, we can conclude that, in particular in the straight section, instantaneous backflow is to a large extent present, while the mean flow is attached.

In figure 6 we show three-dimensional views of $\gamma(\boldsymbol{x})$, where $\boldsymbol{x} = (x, y, z)$. Here, red means $\gamma = 1$, yellow is $\gamma = 0.75$, green is $\gamma = 0.5$ and blue denotes $\gamma = 0$. In figure 6(*a*), $\gamma(\boldsymbol{x})$ is shown in the first point off the two expanding walls, which again qualitatively behaves as the shear stress at the wall. The arrows indicate where ID, ITD and TD occur for the first time in a spanwise midplane, i.e. following the thin black line in figure 5(*b*). As pointed out in Simpson (1989), $\gamma = 0.5$ approximately corresponds to the time-averaged streamwise skin friction being zero (given that the streamwise velocity probability distribution is symmetric about zero velocity), i.e. $\langle \boldsymbol{\tau}_w \cdot \boldsymbol{e}_x \rangle = \boldsymbol{0}$. Here, we can confirm this finding by observing a quantitatively

https://doi.org/10.1017/jfm.2012.107 Published online by Cambridge University Press

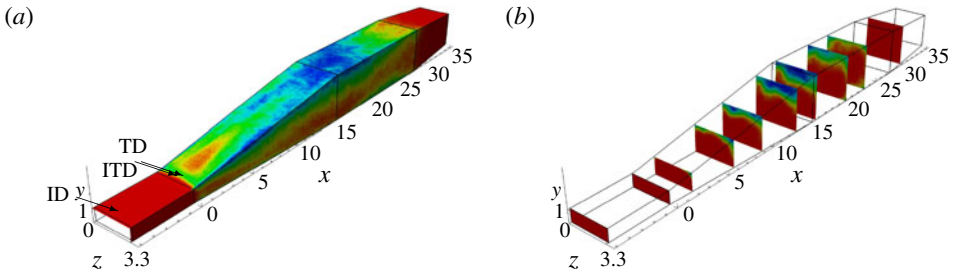


FIGURE 6. Pseudo-colours of $\gamma(\boldsymbol{x})$, ranging from blue for $\gamma = 0$ to red for $\gamma = 1$, shown in (*a*) the first point off the two expanding walls and (*b*) the same cross-flow planes as in figure 2(*b*). Arrows indicate where ID, ITD and TD occur for the first time in a spanwise midplane.

similar shape in the green contour in figure 6(*a*) as in the dotted black line in figure 2(*a*). It is interesting to note that on the upper wall the flow is attached at all times all the way to the diffuser opening (red). Then, there is a short distance where instantaneous backflow occurs (green), noted by Schneider *et al.* (2009) as a region with $U/u_b = 0$. Such a region was not observed in our mean flow data. Shortly thereafter, the flow is in a triangular region 75–90 % of the time (yellow–light red) aligned with the forward direction. To the right of this region, we see an intensely blue area filling the entire upper right edge. Thus, the flow is always oriented in the negative streamwise direction along this edge. Series of instantaneous visualizations of the flow confirm that separated flow further downstream tend to end up in this edge of the diffuser. The triangular region on the upper wall is around $x = 7$ approaching transitory detachment, where $\gamma = 0.5$. This value of $\gamma = 0.5$ is kept in the middle of the upper wall, accompanied by $\gamma \approx 0$ on both sides, until around $x = 15$, where most of the top wall is covered with backflow. This particular behaviour is due to the presence of the 'bump' underneath, clearly visible in figure 6(*b*) (the fifth plane shown), where the same cross-flow planes as in figure 2(*b*) are shown, with the colour scheme being the same as in figure 6(*a*). Here, we also observe the small separated 'triangle' in the upper right corner early in the diffuser (the third plane shown), previously seen in the streamwise mean flow. From both figures 6(*a*) and 6(*b*), we can confirm that most backflow occurs around $x = 15$, as already concluded from figures 5(*a*) and 5(*b*). Further downstream, the flow once again approaches the transitory detachment, i.e. the end of the mean separated region. As soon as the converging section starts, the flow can be seen to be attached 100 % of the time. From an engineering point of view, this shows the efficiency of such a region to counteract separation. Secondly, it points out the importance to include this section for the simulation to mimic the experiment as closely as possible. Without this region, the flow would probably have required a much longer development section in order to become fully attached duct flow again.

3.2. *Observed large-scale oscillations*

As the turbulent flow enters the diffuser, it will rapidly undergo pressure-induced separation. Instantaneous snapshots, such as those depicted in figure 7, indicate that the flow is subjected to a motion that resembles the 'flapping' or meandering of a jet. This feature is strong and has been observed at all times during the simulation. A more quantitative analysis of this phenomenon is made from a set of time signal

https://doi.org/10.1017/jfm.2012.107 Published online by Cambridge University Press

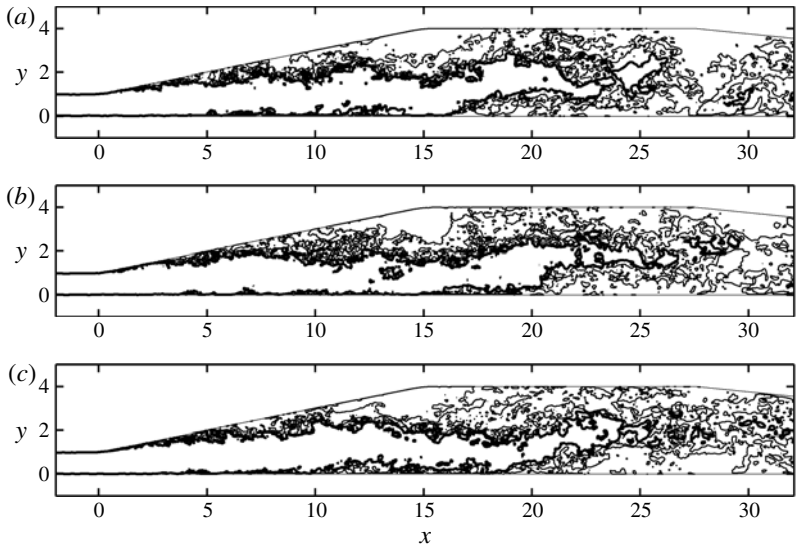


FIGURE 7. Three snapshots in a xy plane at $z = 1.87$ shown at (*a*) $t = t_0$, (*b*) $t = t_0 + 10h/u_b$ and (*c*) $t = t_0 + 20h/u_b$. Thin contour lines of streamwise velocity are shown for $u/u_b = 0,\ 0.2$ and 0.3, whereas the thick contour line is shown for $u/u_b = 0.4$..

probes placed in the flow domain. We have chosen to study the time signal by placing one probe in the upper part and one in the lower part of the diffuser at $x = 5,\ 8,\ 12,\ 15$, where the latter three are indicated in figure 8. These four placings correspond to locations studied for the mean quantities in Cherry *et al.* (2008). The recording of the time signal started well after the flow had reached an equilibrium state and spans a total time of $tu_b/h = 458$, which is enough to capture a few periods of the large-scale oscillations observed in the flow. The time signals are shown in figures 9 and 10, with their respective power spectral density (PSD) shown in figure 11. Except for the close-up view in figure 9(*c*), the interval on the ordinate is fixed to $\Delta u = 0.9u_b$ in all figures to facilitate comparisons. All spectra in the following were computed using Welch's method, where the signal is split into two overlapping segments, each of which is windowed by a Hamming window, whose length is the same as the segment. The spectral resolution in terms of non-dimensional frequency $St \equiv fh/u_b$ is therefore $St = 2/T_{win} = 2/343.5 = 0.0058$, where T_{win} is the length of the windowed signal. The PSD from each signal in figure 11 is normalized by the spectral peak in the time signal given by the upper probe at $x = 15$.

In the symmetric duct (not shown), the flow is governed by rapid velocity fluctuations and small-scale turbulence with a broad spectral content. As we enter the diffuser, the flow quickly becomes different in the upper and lower parts, respectively. Whereas the flow in upper part rapidly loses its highest frequencies, they continue to be present in the fully attached flow close to the lower wall. This is exemplified in figure 9, where the streamwise velocity signal at $x = 8$ in figure 9(*a*) can be seen to have less high spectral content than the signal in figure 9(*d*), which is taken from $x = 12$, i.e. further downstream. At $x = 5$ (only shown in terms of its spectrum in figure 11), a large-scale peak in the upper time signal probe starts to emerge, and we note a peak at $St = 0.044$ besides the one at $St = 0.16$. Still, the small-scale turbulence is significant, evident in figure 11(*c*), where the PSD from the upper probes at $x = 5$

https://doi.org/10.1017/jfm.2012.107 Published online by Cambridge University Press

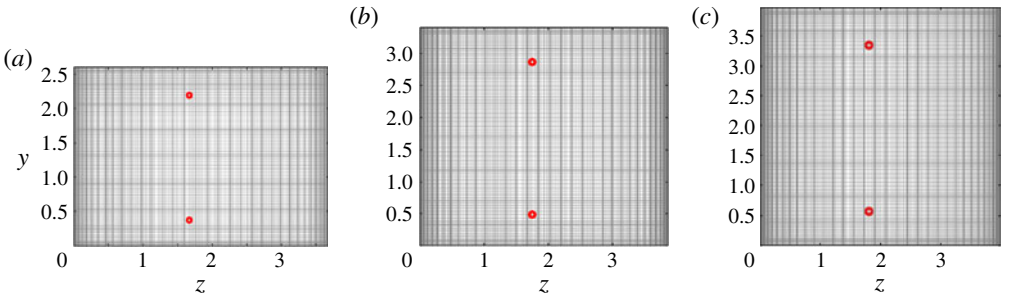


FIGURE 8. Location of history points (thick circles) and computational grid at the streamwise positions (*a*) $x = 8$, (*b*) $x = 12$ and (*c*) $x = 15$.

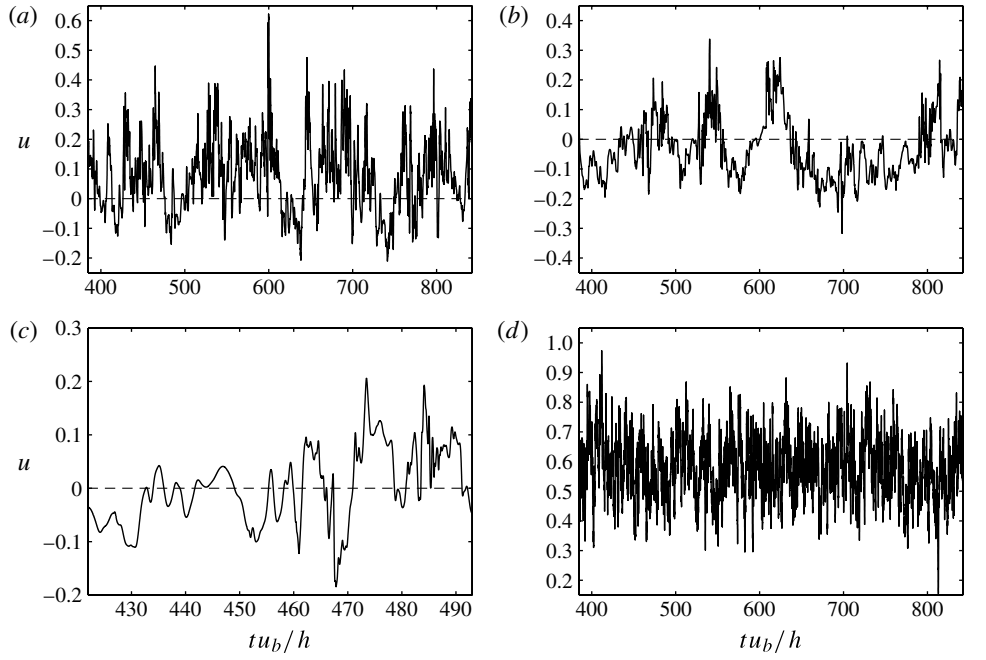


FIGURE 9. Time signals of streamwise velocity from probes located at (*a*) $x = 8$ and (*b*) $x = 12$ in the upper part of the diffuser. (*c*) Close-up view of (*b*) showing the intermittent flow in this region due to the presence of the separation. (*d*) Time signal of streamwise velocity from a probe located at $x = 12$ in the lower part of the diffuser.

and $x = 12$ are compared in a plot with frequencies and energies on a logarithmic scale. As we approach the mean separated region ($x = 8$, figure 9*a*), the strength of the large-scale peak has become significant. Here, the peak at $St = 0.014$ in figure 11(*a*) is three times stronger than the peaks at $x = 5$. This trend continues further downstream, and at $x = 12$, where the time signal is shown in figure 9(*b*), the same peak at $St = 0.014$ is 50 % stronger than it was at $x = 8$. The location of the upper probe at $x = 12$ coincides roughly with the edge of the mean separation bubble as given in Cherry *et al.* (2008) and Ohlsson *et al.* (2010), explaining why in figure 9(*b*) the

https://doi.org/10.1017/jfm.2012.107 Published online by Cambridge University Press

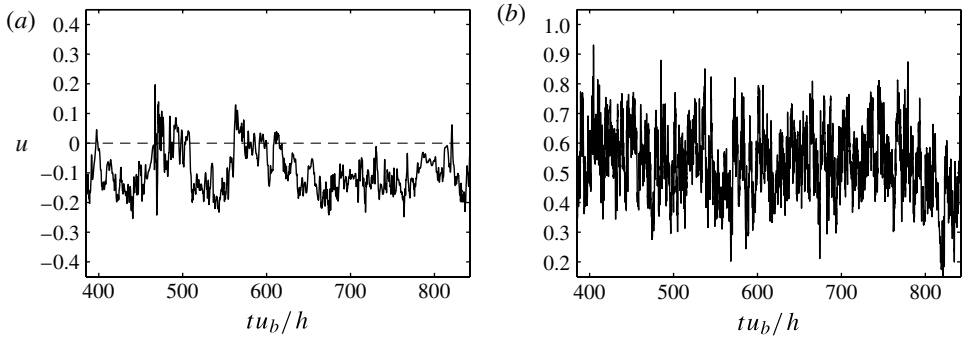


FIGURE 10. Time signals of streamwise velocity from probes located in (*a*) the upper and (*b*) the lower regions of the diffuser at $x = 15$.

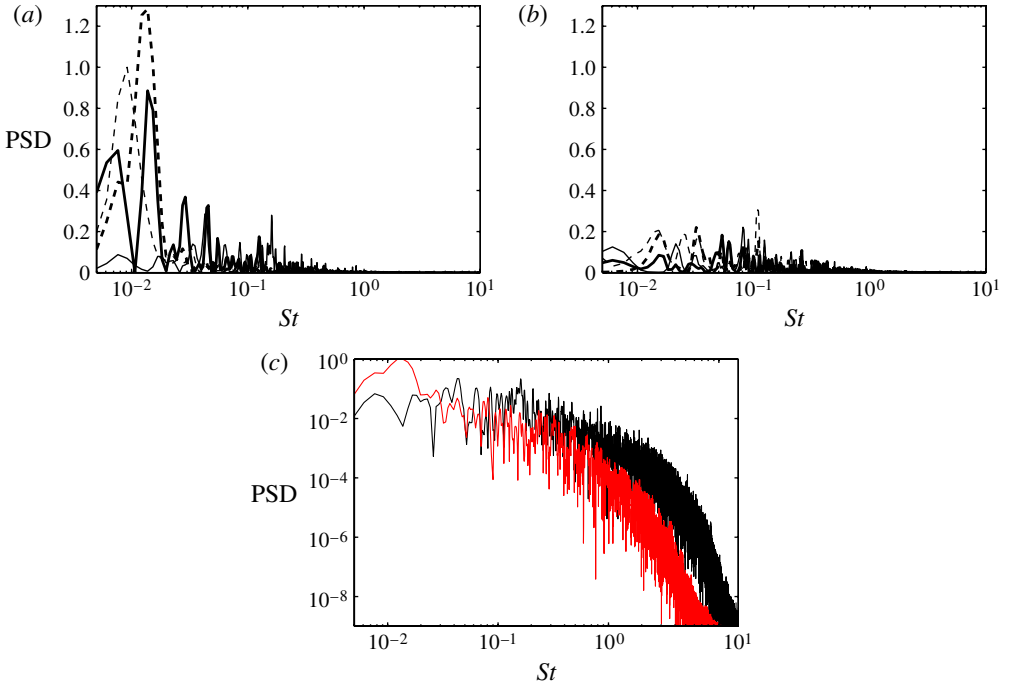


FIGURE 11. Power spectral density (PSD) of the time signals at $x = 5$ (——), $x = 8$ (——), $x = 12$ (– – –) and $x = 15$ (– – –) for (*a*) the upper probe and (*b*) the lower probe, normalized with the maximum intensity of the upper probe at $x = 15$. (*c*) PSD computed from the upper time signal probe at $x = 5$ (black) and $x = 12$ (red).

fluctuations are evenly distributed around zero. Note that the presence of the edge of the separated zone gives rise to a highly intermittent flow, visible in the close-up view in figure 9(*c*). At $x = 15$ the two walls are separated even further apart and the upper probe is now located within the mean separated region. This manifests itself in long periods with negative flow, but also relatively long periods of essentially zero flow, as shown in figure 10(*a*). Still, the spectral peak in figure 11(*a*) is centred around $St \approx 0.01$ ($St = 0.0092$), thus giving an estimate for the frequency of the separated region. The time signal measured by the lower probe is similar to the corresponding

https://doi.org/10.1017/jfm.2012.107 Published online by Cambridge University Press

signal at $x = 12$, except that the magnitude of the mean flow is slightly lower and the spectra in figure 11(*b*) contains somewhat fewer high frequencies. The peak frequency is found at $St \approx 0.1$, i.e. a roughly 10 times higher frequency than the dominant frequency in the separated part of the flow at this streamwise location, but only with approximately a fifth of its magnitude.

To conclude, the analysis from the time probes shows that the flow in the upper part of the diffuser contains large-scale dynamics with dominant frequencies in a comparably narrow band $St \in [0.0092, 0.014]$, yielding time periods $T^* = 1/St \in [70, 110]$, where T^* is a non-dimensional time. The fact that there is a narrow band of dominant frequencies seen in the separated part of the diffuser suggests that there may be self-sustained oscillations present, since there is a possibility for disturbances to create a feedback mechanism via the recirculated flow. This is supported by the findings of Lawson & Davidson (2001) and Villermaux & Hopfinger (1994), who found self-sustained oscillations to be present in confined jets in conjunction with adjacent separated zones. At this point it is important to note that, in studies of two-dimensional diffuser geometries (Kaltenbach *et al.* 1999; Herbst *et al.* 2007), flat spectra without any distinct peaks were observed.

4. Analysis of modal decomposition

4.1. *Flow decomposition*

The large-scale oscillations observed in the time probes indicate that there might be large-scale energetic and coherent structures present in the flow. To investigate this further, POD is used to decompose the flow into its most energetic three-dimensional parts (Lumley 1967; Holmes, Lumley & Berkooz 1996). Considering the turbulent flow field $\boldsymbol{u}(\boldsymbol{x}, t)$ with velocity vector $\boldsymbol{u} = (u, v, w)$, defined in physical space $\boldsymbol{x} = (x, y, z)$ and time t, a modal decomposition of this kind attempts to split the space and time dependences, and is thus of the form

$$\boldsymbol{u}(\boldsymbol{x}, t) = \sum_{j=0}^{\infty} a_j(t)\boldsymbol{\psi}_j(\boldsymbol{x}). \tag{4.1}$$

Note that $\boldsymbol{u}(\boldsymbol{x}, t)$ indeed is the full velocity field, i.e. the mean flow not being subtracted. As we shall soon see, the implication for the POD is that the mean flow will be part of the decomposition. Since our velocity fields are naturally truncated by the numerical simulation, this sum can, without loss of generality, be taken up to some $m \ll \infty$. The POD procedure finds deterministic, bi-orthogonal functions, $\boldsymbol{\psi}_j(\boldsymbol{x})$, that maximize the energy in the field $\boldsymbol{u}$. A necessary condition for this to hold is that $\boldsymbol{\psi}_j(\boldsymbol{x})$ is an eigenfunction of the two-point spatial correlation tensor $\boldsymbol{R}(\boldsymbol{x}, \boldsymbol{x}') = \int_T \boldsymbol{u}(\boldsymbol{x}, t)\boldsymbol{u}(\boldsymbol{x}', t)\,\mathrm{d}t/T$, where T denotes the total time over which the flow is observed (rigorously shown in Holmes *et al.* 1996). Finding the eigenvalues, λ_j, and corresponding eigenfunctions, $\boldsymbol{\psi}_j$, of $\boldsymbol{R}(\boldsymbol{x}, \boldsymbol{x}')$ amounts to solving

$$\iiint_V \boldsymbol{R}(\boldsymbol{x}, \boldsymbol{x}')\boldsymbol{\psi}_j(\boldsymbol{x}')\,\mathrm{d}\boldsymbol{x}' = \lambda_j\boldsymbol{\psi}_j(\boldsymbol{x}). \tag{4.2}$$

The m temporal coefficients at m discrete times in (4.1) can then, in a successive step, be solved for by projecting the spatial modes onto the velocity field,

$$a_j(t) = \iiint_V \boldsymbol{u}(\boldsymbol{x}, t)\boldsymbol{\psi}_j(\boldsymbol{x})\,\mathrm{d}\boldsymbol{x}, \tag{4.3}$$

https://doi.org/10.1017/jfm.2012.107 Published online by Cambridge University Press

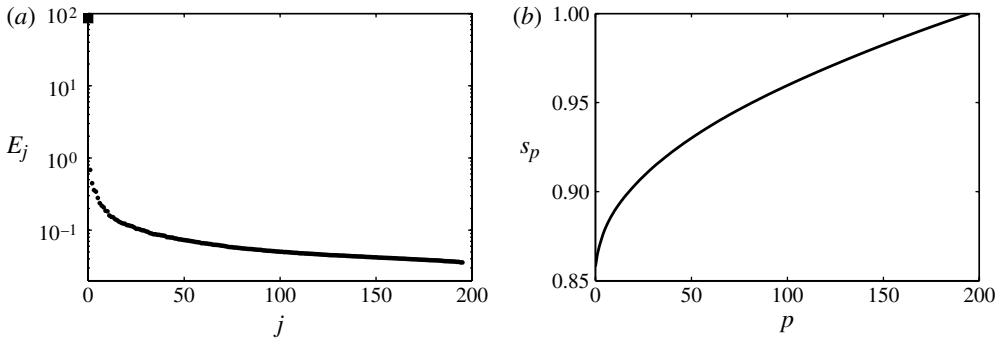


FIGURE 12. (*a*) The total kinetic energy $E_j = \left(\lambda_j / \sum_{i=0}^{195} \lambda_i\right) \times 100$ of the POD modes with $j = 0, \ldots, 195$. The mean flow ($j = 0$) is indicated by the solid square. (*b*) Cumulative energy sum, $s_p = \sum_{i=0}^{p} \lambda_i$, for modes $p = 0, 1, \ldots, 195$ in the expansion.

where we have used the bi-orthogonality in space. Note that the discrete equivalent of $\boldsymbol{R}$ will be a matrix of size $n \times n$, where $n = 3 \times n_x \times n_y \times n_z$, and n_x, n_y and n_z are the resolutions in the spatial directions, respectively. Therefore, for high spatial resolutions, (4.2) is usually impossible to solve directly. However, using the snapshot method (Sirovich 1987), (4.2) can be circumvented by solving an eigenvalue problem of the generally smaller temporal two-point correlation tensor $\boldsymbol{C}(t, t') = \iiint_V \boldsymbol{u}(\boldsymbol{x}, t)\boldsymbol{u}(\boldsymbol{x}, t')\,\mathrm{d}\boldsymbol{x}/T$, which is computed using a sequence of flow fields or 'snapshots' saved at m discrete times $\{\boldsymbol{u}(t_1), \ldots, \boldsymbol{u}(t_m)\}$. This yields a matrix of size $n \times m$, which for numerical simulations is typically smaller than $n \times n$. We are now instead solving

$$\int_T \boldsymbol{C}(t, t') a_j(t')\,\mathrm{d}t' = \lambda_j a_j(t). \tag{4.4}$$

Then, as a second step, the spatial eigenfunctions are constructed as

$$\boldsymbol{\psi}_j(\boldsymbol{x}) = \frac{1}{T\lambda_j} \int_T a_j(t)\boldsymbol{u}(\boldsymbol{x}, t)\,\mathrm{d}t. \tag{4.5}$$

Here, the division by the respective eigenvalue ensures that the modes are normalized to unit energy. Once this is done, the temporal coefficients can be computed according to (4.3), and the ones obtained from (4.4) are disregarded.

For the present POD analysis, a set of $m = 196$ snapshots spanning a time of $\Delta t u_b/h = 392$ is used. The temporal resolution is set to $\Delta t u_b/h = 2$. It has been verified that the mean flow and the mean fluctuations of these snapshots are in close agreement with the results in Ohlsson *et al.* (2010), and thus the experimental data by Cherry *et al.* (2008). A discussion regarding convergence of the POD modes is given at the end of the present section. To avoid (4.4) being prohibitively expensive to solve, the streamwise extent of the velocity fields was reduced, such that only data between $x = -0.15$ and $x = 23.85$ were used for the POD analysis. After this operation, the resulting matrix containing all snapshots has size $n \times m \sim 10^9$, where $n = 3 \times n_x \times n_y \times n_z = 3 \times 1152 \times 120 \times 420 \approx 1.74 \times 10^8$ and $m = 196$. Assuming each entry in the matrix being of double-precision accuracy yields a matrix of size ~273 GB.

https://doi.org/10.1017/jfm.2012.107 Published online by Cambridge University Press

Group	Mode (s)	E_j^{fluct} (%)	$St \equiv fh/u_b$	λ_x	λ_y	λ_z
A	1–6	16.5	0.005–0.015	$10h$	$4h$	$4h$
B	7–16	11.7	0.01–0.04	$2.5h$	$2h$	$2h$
C	17–195	71.7	0.04–0.3	$\leqslant 2.5h$	$\leqslant 2h$	$\leqslant 2h$

TABLE 2. Characteristics of the various groups of POD modes.

The fraction of energy in the respective modes is given by $E_j = \left(\lambda_j / \sum_{i=0}^{195} \lambda_i\right) \times 100$, with $j = 0, \ldots, 195$ and λ_j being the eigenvalues. The entire energy spectrum is shown in figure 12(*a*). Since the mean was not subtracted from the flow fields prior to the decomposition, the first mode in the expansion containing most of the kinetic energy (indicated by the black square) is the mean flow, denoted by 'mode 0'. The cumulative energy sum, $s_p = \sum_{i=0}^{p} \lambda_i$, is shown in figure 12(*b*), from which we can conclude that the mean flow carries the bulk, approximately 86 %, of the kinetic energy. This is close to what was found for a POD of a fully inhomogeneous turbulent flow over a surface-mounted obstacle by Manhart & Wengle (1993), who noted that 91.4 % of the total kinetic energy was contained in the mean flow. In figure 12(*b*) we also note that the last 90 % of the modes contribute as little as 10 % to the total energy. Since the mean flow is not the main topic of the present section, the discussion will from now on focus on the fluctuating modes. The fluctuating energy, defined as $E_j^{fluct} = \left(\lambda_j / \sum_{i=1}^{195} \lambda_i\right) \times 100$, with $j = 1, \ldots, 195$, is shown in figure 13(*a*). The corresponding cumulative energy sum, $s_p^{fluct} = \sum_{i=1}^{p} \lambda_i$, is shown in figure 13(*b*). From figure 13(*a*), we see that the first, second and third modes contribute 4.8, 3.1 and 2.5 %, respectively, to the fluctuating kinetic energy. Moreover, $E_1^{fluct}/E_2^{fluct} = 1.5$ and $E_2^{fluct}/E_3^{fluct} = 1.2$, which is similar to Moin & Moser (1989) for their POD analysis of a turbulent channel flow. However, there, the first mode contained approximately 50 % of the fluctuating energy. For the present case, the results are more in line with Manhart & Wengle (1993), where no dominant modes (in terms of energy) could be found by the POD. Based on their typical frequencies and wavelengths (to be discussed in a moment), the fluctuating modes are divided into three groups. Note that this division is arbitrary but indeed captures the characteristic energy contributions of the modes to the total energy. The groups are labelled A, B and C and listed in table 2. Further, they are indicated in figure 13(*a*) by different symbols. We observe that this division roughly coincides with the change of slope of the spectrum, which happens approximately in the junction between groups B and C. In group C, the energy distribution is flatter and the modes are consequently less distinct and more related to smaller-scale turbulence. Figure 13(*b*) suggests further that approximately 25 % (49 out of 195) of the fluctuating modes are needed to represent 50 % of the fluctuating energy, which is typically observed to be the case for turbulent flows (e.g. Manhart & Wengle 1993). From figure 13(*a*), it is evident that the modes do not pairwise occupy exactly the same energy as would be the case for a POD decomposition of a linear flow, where pure travelling structures are commonly present. As we shall see, however, this does not rule out the fact that a travelling coherent structure exists in the present flow.

Three-dimensional visualizations of POD modes 1, 2 and modes 3, 8 are given in figures 14 and 15, respectively. Modes 1, 2, 3 are representative for group A, whereas mode 8 is characteristic for group B. In terms of energy, modes 1 and 8 are related

https://doi.org/10.1017/jfm.2012.107 Published online by Cambridge University Press

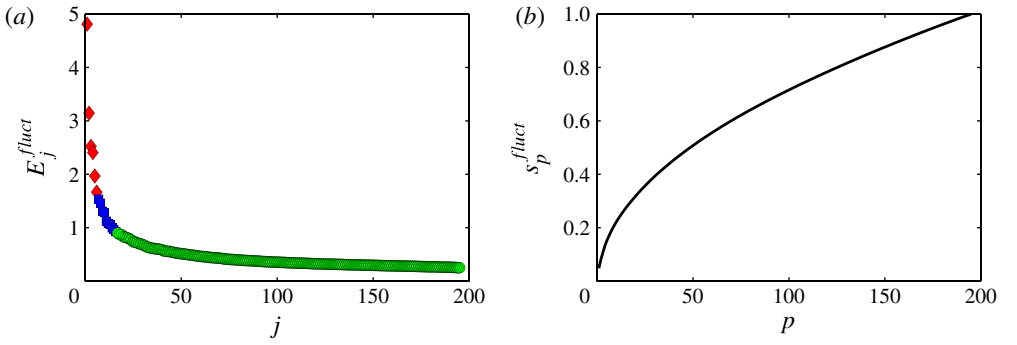


FIGURE 13. (*a*) The fluctuating kinetic energy $E_j^{fluct} = (\lambda_j / \sum_{i=1}^{195} \lambda_i) \times 100$ with $j = 1, \ldots, 195$, where the groups in table 2 are indicated by: $\diamond$, A; $\square$, B; and $\circ$, C. (*b*) Cumulative energy sum of the fluctuating kinetic energy, $s_p^{fluct} = \sum_{i=1}^{p} \lambda_i$.

as $E_1^{fluct}/E_8^{fluct} = 3.3$. A number of important observations can be made. First of all, the structures corresponding to the first three fluctuating modes are essentially two large streamwise streaks, with alternating positive and negative streamwise fluctuation velocity. The magnitude of their streamwise velocity component is roughly 500 times the cross-flow velocities. The combined effect of these fluctuations is to bend the confined jet and create a streamwise wave. The corresponding wavelength is estimated to be $\lambda_x \approx 10h$. In the two cross-stream directions (y and z), the modes span the entire cross-section, such that $\lambda_y = \lambda_z \approx 4h$. These structures are thus the largest possible for the given geometry, since $L_y = L_z = 4h$ in the region where the modes are active. This is in agreement with Villermaux & Hopfinger (1994), who concluded that, for confined flapping jets in asymmetric configurations, the largest confinement dimension will dominate the flow. The streaks in figure 14 resemble the POD modes originating from a jet with inherent low-frequency flapping (see Moreno *et al.* 2004), supporting the fact that there is indeed a sinusoidal motion present in the diffuser. Note that the modes here are shown at one specific time, and, since each mode has a particular time dependence given by the (approximately) sinusoidal variation (to be discussed shortly), the wave has at some later time shifted its positive and negative sides. Indeed, the streamwise wavelength noted above is consistent with the meandering visible in the instantaneous snapshots in figure 7. One of the streaks pertaining to mode 1 (figure 14*a*) is filling the right lower corner ① (when facing in the positive x direction). The second streak in this mode is located above the first one and centred in the domain with respect to z ②, implying a diagonal wave motion in this region. Mode 2, on the other hand, appears to be located half a wavelength upstream of mode 1. In particular, one of its streaks continues upstream of the recently mentioned streak of mode 1 ③. Likewise, its second streak is somewhat upstream of the first described streak of mode 1 and situated very close to the right wall in the diffuser ④. Both modes extend into the mean separated region (cf. the mean flow in figure 2*a*), implying a coherent movement of the flow inside and outside the mean separated region. Mode 3 (figure 15*a*) displays a very clear wave, whose oscillation mainly goes along z, since negative ⑤ and positive ⑥ fluctuations are located side by side in the z direction.

Higher modes, e.g. mode 8 (see figure 15*b*), have wavelengths approximately half that of the first four modes, in terms of both the streamwise and spanwise (i.e. y and

https://doi.org/10.1017/jfm.2012.107 Published online by Cambridge University Press

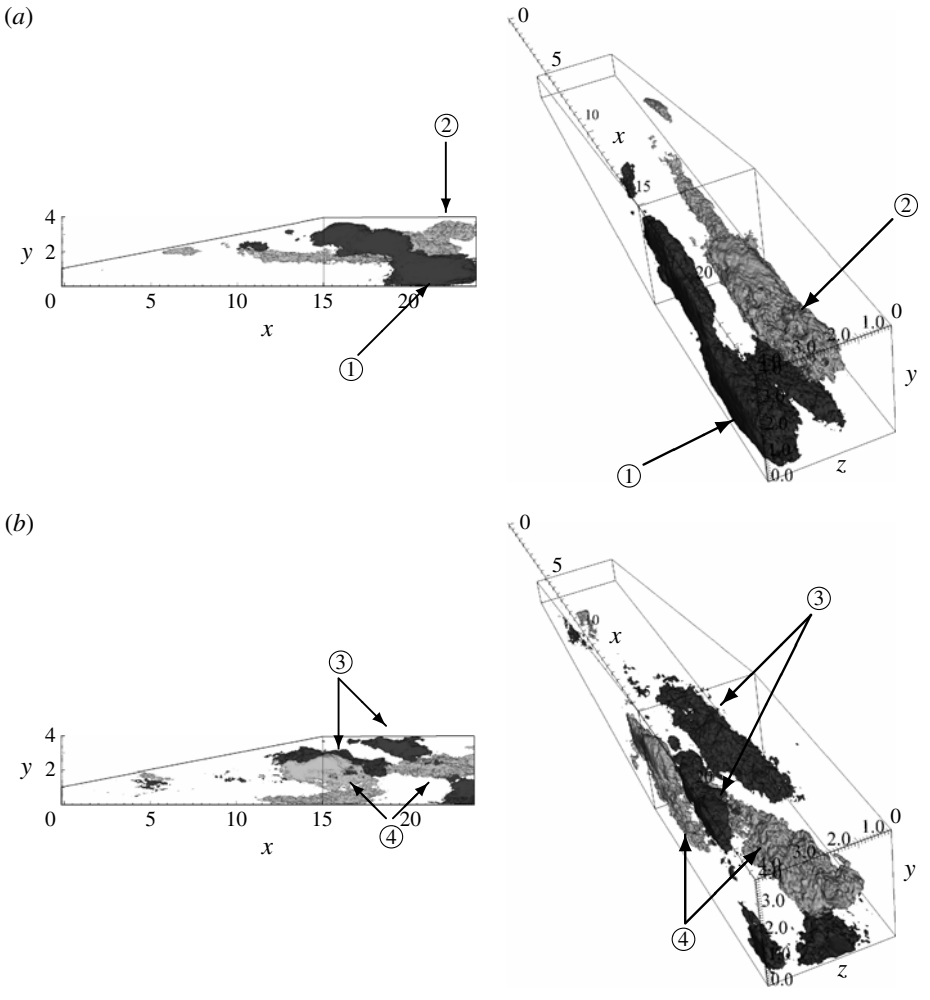


FIGURE 14. Isosurfaces (dark grey, 0.1; light grey, −0.1) of streamwise velocity pertaining to (*a*) POD mode 1 and (*b*) mode 2, shown at two different angles. The numbers indicate specific structures of the respective modes, which are described further in the text.

z) wavelengths, respectively. They are in general more spread throughout the diffuser, but are mainly located upstream of the previous modes. Correspondingly, mode 8 is observed to extend very little beyond $x \approx 15$ in figure 15(*b*). Owing to the location of the positive ⑦ and negative ⑧ fluctuations, this suggests a spanwise flapping mainly located within the diffuser region. In the side view in figure 15(*b*), we note that mode 8 does not extend into the mean separated region as much as the previous modes, which indicates that the separated zone shares its dominant frequency rather with the largest structures in the diffuser.

The time dependence of the POD modes is computed by Galerkin projection (equation (4.3)) and shown in figure 16(*a–c*). Note that the time axes have been redefined such that $t' u_b/h = 0$ in these figures denotes the actual time $tu_b/h = 448$, when saving of instantaneous snapshots was initiated (see table 1). At least for the largest structures (figure 16*a*,*b*), the behaviour is nearly sinusoidal. We observe

https://doi.org/10.1017/jfm.2012.107 Published online by Cambridge University Press

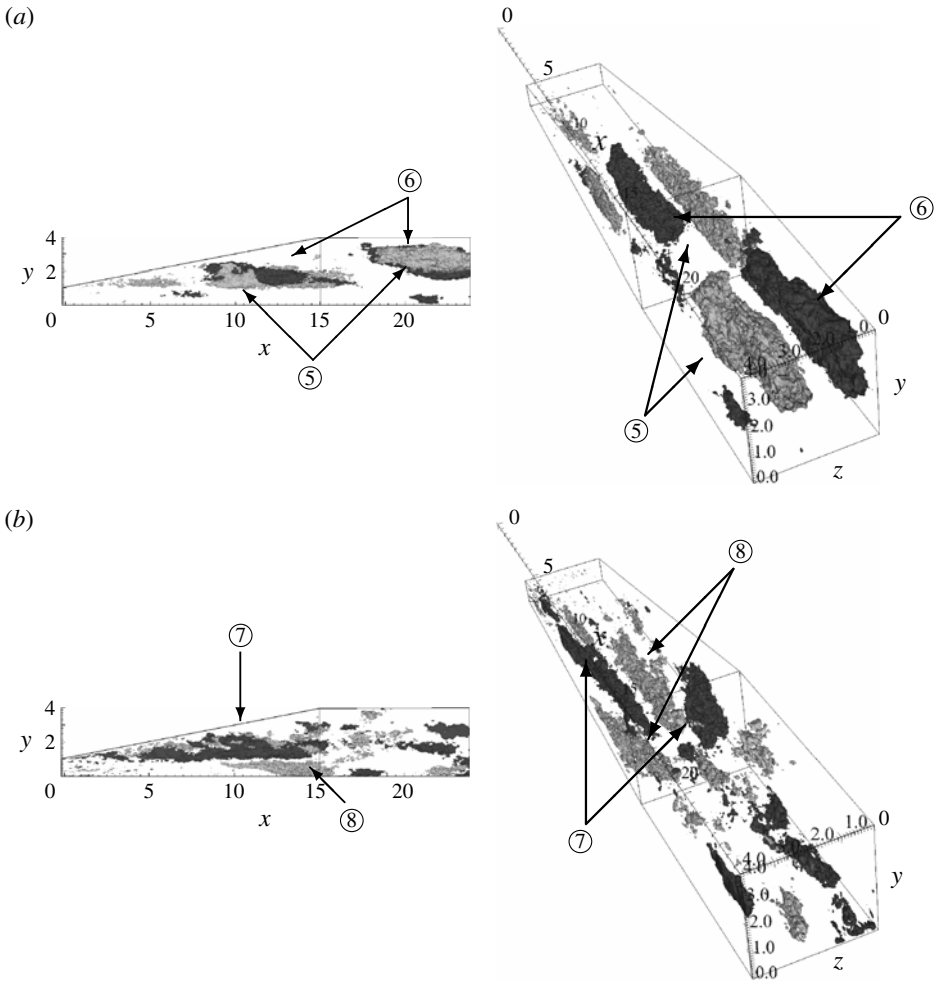


FIGURE 15. Isosurfaces (dark grey, 0.1; light grey, −0.1) of streamwise velocity pertaining to (*a*) POD mode 3 and (*b*) mode 8, shown at two different angles. The numbers indicate specific structures of the respective modes, which are described further in the text.

approximately four periods in figure 16(*a*), whose length can be estimated by $T \sim 100h/u_b$, giving a non-dimensional period of $T^* = Tu_b/h \sim 100$. The corresponding Strouhal number is therefore $St = 1/T^* \sim 0.01$. This frequency compares well to the spectral peak of the PSD in figure 11(*a*). Approximately the same period can be deduced from the evolution pertaining to modes 3 and 4 in figure 16(*b*). Considerably more revolutions (∼12, i.e. three times more) are visible for modes 8 and 9 in figure 16(*c*), which roughly corresponds to the spectral peaks with higher frequency around $St = 0.04$ in figure 11(*a*).

A graphical representation of how the energy is distributed among the various fluctuating modes is given in figure 17. The colours show the logarithm of the modal energy, with the maximum of the first fluctuating mode normalized to unity. We see an accumulation of energy in the low-frequency range, mainly in a band around $St = 0.01$. Clearly, these first modes are lacking energy in the high-frequency range.

https://doi.org/10.1017/jfm.2012.107 Published online by Cambridge University Press

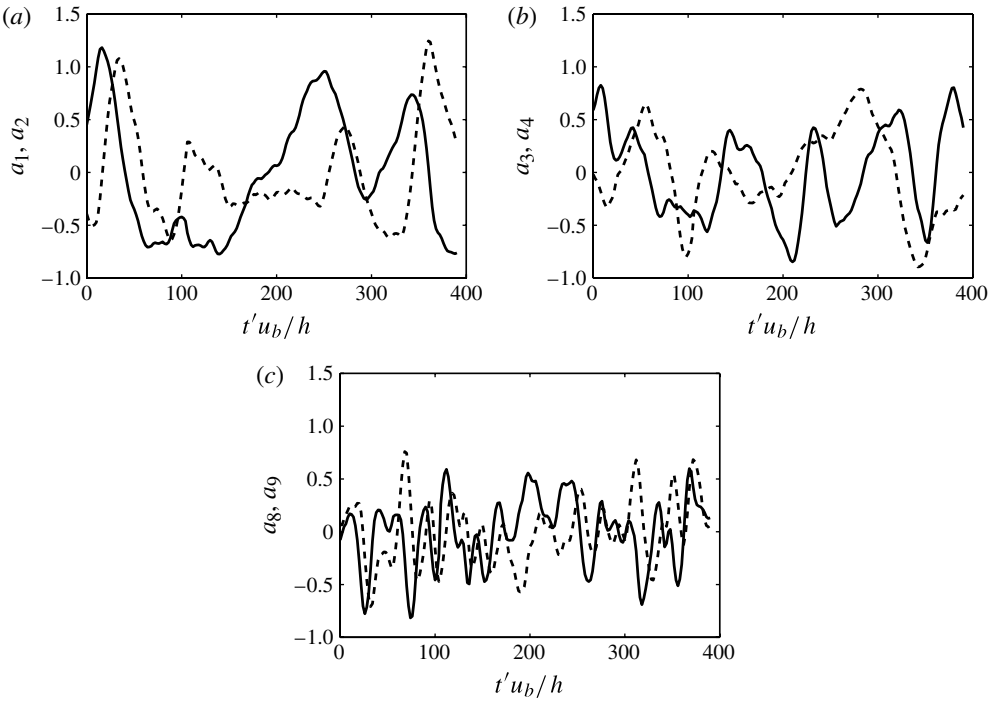


FIGURE 16. Temporal evolution of (*a*) modes 1 (——) and 2 (– – –), (*b*) modes 3 (——) and 4 (– – –) and (*c*) modes 8 (——) and 9 (– – –).

Higher modes, on the other hand, have little energy in the low-frequency range, which indicates that each of the different modes is relatively localized in frequency space. This localization typically benefits the use of Koopman modes (see Rowley *et al.* 2009) for the flow analysis. This approach enables one specific structure to be associated with one specific frequency. However, we have chosen the more well-established POD route, since it usually provides smoother structures in turbulent flows. Finally, as noted before, in conjunction with figure 13, we see that the energy in figure 17 is quite well distributed among the various scales, with roughly one order of magnitude in energy from the largest to the smallest scales.

In order to reveal the existence of travelling waves in the diffuser, we will next project the flow onto the two-dimensional phase space spanned by the fluctuating POD modes at hand, i.e. the time evolution of modes i and j (computed by (4.3)) are drawn simultaneously. A wave in its most simple form may be completely characterized by two modes shifted 90° in time. The two-dimensional phase portraits would in this case correspond to a circle, i.e. a periodic orbit, $\boldsymbol{r}(t) = a_i(t)\boldsymbol{\psi}_i + a_j(t)\boldsymbol{\psi}_j = A\cos(t)\boldsymbol{e_x} + A\sin(t)\boldsymbol{e_y}$, where A is the amplitude of the mode and t is the time. If the time axis is included as a third direction, the resulting parametrized curve would be a helix, mathematically described by $\boldsymbol{r}(t) = A\cos(t)\boldsymbol{e_x} + A\sin(t)\boldsymbol{e_y} + t\boldsymbol{e_z}$. On the other hand, no particular coherence would correspond to a joint probability density function (p.d.f.) of two random variables, uniformly distributed between $-A/2$ and $A/2$. If the time signal was not exactly periodic, i.e. quasi-periodic, the circle would not be closed, but rather would spiral either inwards or outwards. In figure 18, the two-dimensional projection is shown for the fluctuating POD modes discussed above. In

https://doi.org/10.1017/jfm.2012.107 Published online by Cambridge University Press

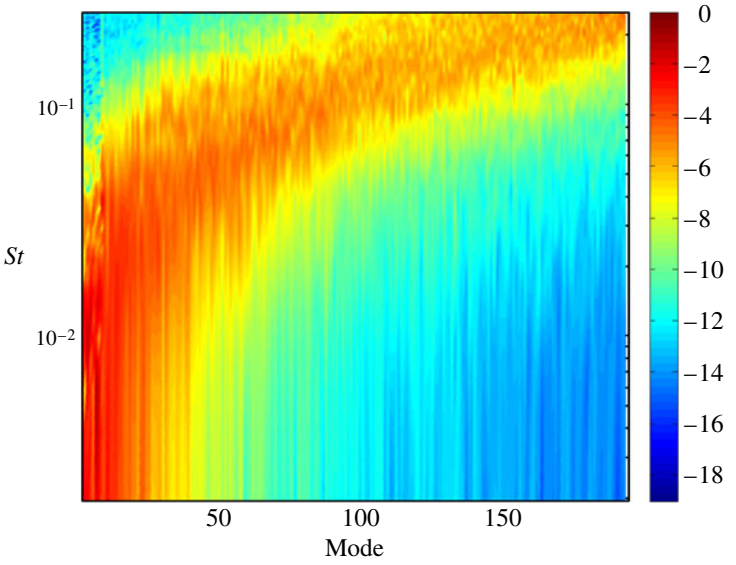


FIGURE 17. Energy distribution among the various fluctuating modes normalized by the peak value of the first fluctuating mode. The colours show the logarithm of the power spectral density of the respective modes.

particular, figures 18(*a*,*b*) and 18(*c*,*d*) show the trajectories in the subspaces ($\boldsymbol{\psi}_1$, $\boldsymbol{\psi}_2$) and ($\boldsymbol{\psi}_8$, $\boldsymbol{\psi}_9$), respectively. Time is increasing anticlockwise in all figures, starting at t_0 and ending at t_{end}. In figure 18(*b*,*d*) the time axis is included as a third direction. Considering the high turbulence levels of the present flow (u_{rms}/u_b up to 25 %), these phase portraits show a remarkable coherence. The trajectory in figure 18(*a*) completes slightly more than three revolutions. The fact that the revolutions are not on top of each other merely indicates that each oscillation is not exactly the same, but nevertheless at least three cycles are present, more easily seen in figure 18(*b*). In figure 18(*c*), corresponding to modes 8 and 9, approximately 10 revolutions are present, which are closely on top of each other. Including time as a third direction in figure 18(*d*), we see that the motion approximately takes the form of a helix, hence the revolutions are linear in t. The radius of the helix can be seen to change somewhat, which is an effect of the modes not being fully separated in frequency space and consequently containing some lower frequencies. In other words, it indicates that the dynamical interaction of the modes is more complex than a pair of modes exchanging energy, which is also reasonable to expect. This finding gives a strong indication of the quasi-periodic motion in the diffuser that gives rise to a travelling wave. Two typical frequencies of approximately $St = 0.01$ and $St = 0.04$ have been shown to be active. The convection velocities, v_p, of these waves can be computed approximately using the wavelengths and frequencies given in table 1. Using the expression for phase velocity, we find $v_p = f\lambda_x \sim 0.01 \times 10 \sim 0.04 \times 2.5 \approx 0.1$, which is of the same order of magnitude as can be deduced from the snapshots in figure 7. Note that the number of complete revolutions seen in figure 18(*a*,*b*) and the periods derived from figure 16 are limited but nonetheless ensured to be correct, as the same frequencies have been observed in the entire data set, including earlier simulation times not shown here.

https://doi.org/10.1017/jfm.2012.107 Published online by Cambridge University Press

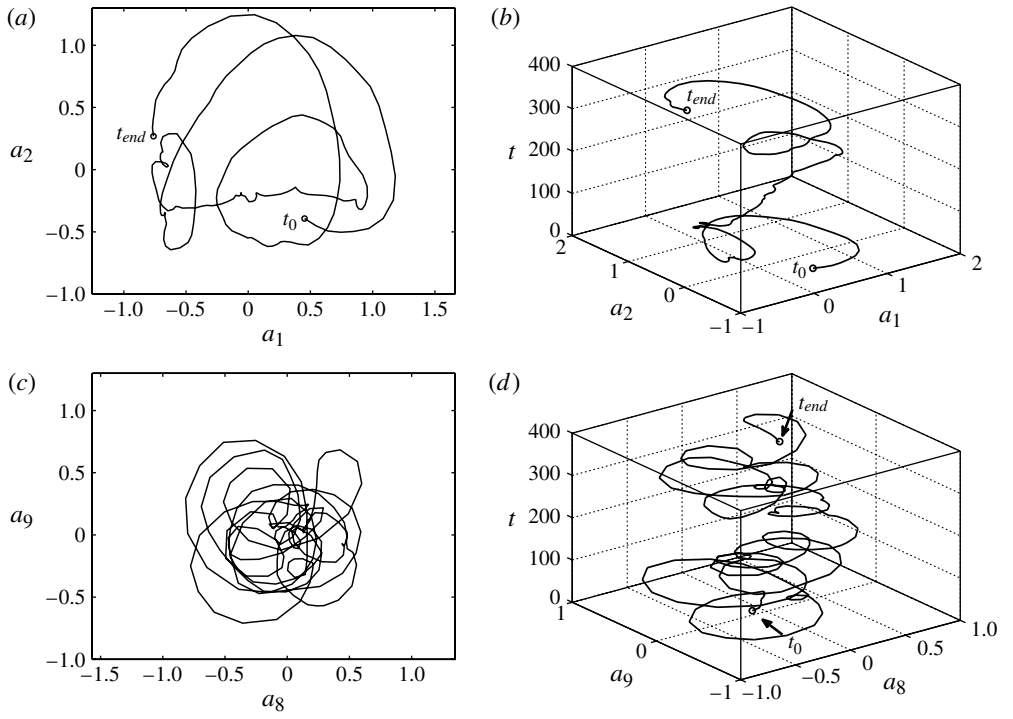


FIGURE 18. Temporal orbits in the subspaces (*a*) ($\boldsymbol{\psi}_1, \boldsymbol{\psi}_2$) and (*b*) ($\boldsymbol{\psi}_8, \boldsymbol{\psi}_9$) showing the quasi-periodic motions of the largest and second largest structures present in the diffuser, respectively. In panels (*a*) and (*c*), time is increasing anticlockwise. In panels (*b*) and (*d*), the motion is shown along the vertical time axis.

In summary, the POD analysis of the present data has not identified any dominant structure, except for the mean flow, in terms of energy. In spite of this, the first eigenfunctions are large structures with a high degree of spatial coherence, which moreover display a quasi-periodic temporal behaviour. They are consequently important in order to explain the dynamics in the diffuser. Similar structures with similar time dependence were identified by Moreno *et al.* (2004) in an experimental study of a turbulent jet. There, however, a larger fraction of the total energy was contained in the first two modes.

A final remark on the convergence of the POD modes is necessary. Ideally, as more and more snapshots are included, the eigenvalues λ_j from problem (4.4) and the eigenfunctions $\boldsymbol{\psi}_j(\boldsymbol{x})$ from (4.5) should converge. For a flat spectrum, such as the one reported in figure 12, many thousands of snapshots are needed to converge the eigenvalues (see Manhart & Wengle 1993). The first eigenfunctions of the POD, on the other hand, generally converge much quicker. Since this study aims at quantifying the observed large-scale motion, we limit ourselves to establishing convergence of the first few modes. This can be undertaken by an orthogonality check between the modes. Since POD modes are orthogonal to each other by construction,

$$\iiint_V \boldsymbol{\psi}_j(\boldsymbol{x})\boldsymbol{\psi}_i(\boldsymbol{x})\,\mathrm{d}\boldsymbol{x} = \delta_{ij}, \tag{4.6}$$

https://doi.org/10.1017/jfm.2012.107 Published online by Cambridge University Press

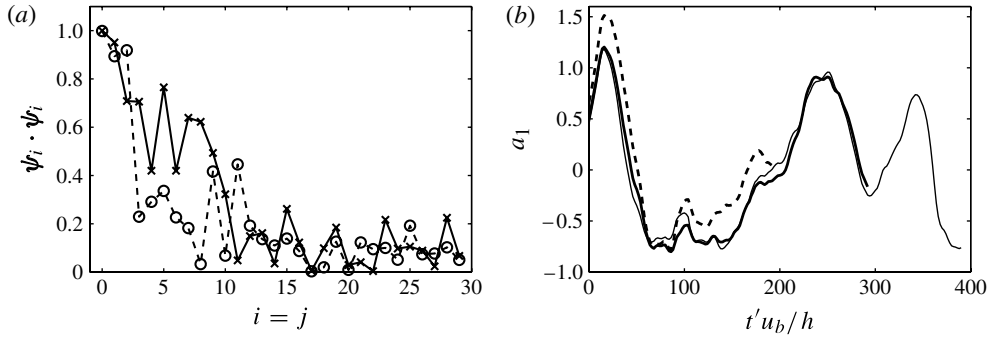


FIGURE 19. Convergence of the POD modes. (*a*) The inner product between the 30 first modes computed with 98 and 147 snapshots (– – –) and 147 and 196 snapshots (——), respectively. Only $i = j$ is shown, with 1 indicating parallel and 0 indicating orthogonal vectors. (*b*) Time evolution of POD mode 1 computed with 98 (——), 147 (– – –) and 196 (——) snapshots.

where δ_{ij} is the Kronecker delta, holds exactly. If in (4.6) we used modes computed using 98 and 147, or 147 and 196, snapshots, we would get a measure for the convergence, i.e.

$$\iiint_V \boldsymbol{\psi}_j^{98\ snaps}(\boldsymbol{x})\boldsymbol{\psi}_i^{147\ snaps}(\boldsymbol{x})\,\mathrm{d}\boldsymbol{x} = \widetilde{\delta}_{ij}^{1}, \tag{4.7}$$

or

$$\iiint_V \boldsymbol{\psi}_j^{147\ snaps}(\boldsymbol{x})\boldsymbol{\psi}_i^{196\ snaps}(\boldsymbol{x})\,\mathrm{d}\boldsymbol{x} = \widetilde{\delta}_{ij}^{2}, \tag{4.8}$$

respectively. Here, $\widetilde{\delta}_{ij}$ denotes the approximate Kronecker delta. In figure 19(*a*), we compare $\widetilde{\delta}_{ij}^{1}$ and $\widetilde{\delta}_{ij}^{2}$ for $i = j$. Clearly, $\widetilde{\delta}_{ii}^{2}$ (no summation on repeated indices) are closer to unity than $\widetilde{\delta}_{ii}^{1}$, indicating that the structures change less by adding 49 more snapshots to 147 than to 98. Moreover, the inner product between $\boldsymbol{\psi}_j^{147\ snaps}$ and $\boldsymbol{\psi}_j^{196\ snaps}$ shows a value of 0.7 for the first four modes, suggesting that the modes do not change much, even if the data sets are spaced 49 snapshots apart, i.e. approximately one of the long periods discussed earlier. A similar check is performed using the time series of mode 1, computed using 98, 147 and 196 snapshots, shown in figure 19(*b*). If the mode is unchanged, then the time series is expected to be identical. We observe that the evolution changes by employing 147 instead of 98 snapshots. However, the change is minor as 49 additional snapshots (i.e. a total of 196) are used. For inflow–outflow problems, such as the present flow, the modes are not generally phase-shifted, and consequently orthogonality in space is a valid measure of the convergence of the structures. We therefore conclude that 196 snapshots are enough for the proper orthogonal decomposition in order to get a correct representation of the large-scale spatial structures.

4.2. *Low-dimensional reconstruction*

The scale separation provided by the POD suggests studying the large-scale anisotropic dynamics without the influence of the small-scale turbulence in a ‘low-pass filtered’ manner. Hence it facilitates the focus on the relevant dynamics and helps us in

https://doi.org/10.1017/jfm.2012.107 Published online by Cambridge University Press

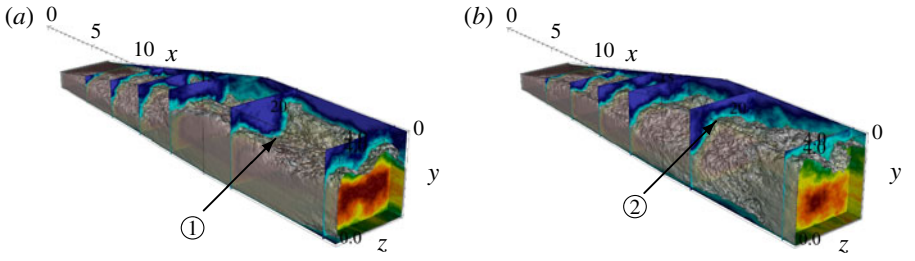


FIGURE 20. Superposition of POD modes 0–6 shown for one period in figure 16(*a*) at times (*a*) $tu_b/h = 8$ and (*b*) $tu_b/h = 54$. The grey isosurface shows constant streamwise velocity, $u/u_b = 0.1$. Cross-flow planes show streamwise velocity ranging from -0.1 (blue) to 0.5 (red).

our physical understanding of the dominant dynamical processes in the flow. To build the low-pass filtered (i.e. low-dimensional) model, we follow the procedure previously employed in, for example, Cazemier, Verstappen & Veldman (1998, and references therein) by superimposing some of the first modes in the expansion, here modes 0–6, with their corresponding temporal weight and studying the time evolution. Mode 0 is the mean flow, and contains most of the energy in the diffuser, as discussed previously. Modes 1–6 belong to 'group A' where the largest wavelengths and lowest frequencies are found. Therefore, these modes are representative for the large-scale motion in the diffuser, and thus the focus of the present study. Isosurfaces of constant streamwise velocity are shown in figure 20 at two specific times ($t'u_b/h = 8$ and $t'u_b/h = 54$). The travelling wave shown in the phase portraits is now clearly seen to propagate through the domain. Starting from figure 20(*a*), the sinusoidal shape of the high-speed core of the flow has one of its minima located at $x \approx 20$ ①. As a consequence of the confinement of the flow, high-velocity fluid is pushed up on the sides, close to the sidewalls. One half-period later, in figure 20(*b*), the minimum has propagated forwards in the domain (not visible any more), and is now replaced by a maximum at $x = 20$ ②. Again, the confinement forces the flow in a cross-flow plane downwards in the vicinity of the sidewalls. Another half-period later (not shown) the flow is back to its approximate original state. To conclude, the low-dimensional model translates the quasi-periodic motion exemplified in the phase portrait in figure 18(*a*,*b*) into flow variables, and the travelling wave is clearly visible. An effect of this meandering is a strong secondary flow created in the cross-flow directions. Thus, relating back to the mean vorticity in figure 4, the unsteady jet motion will generate negative streamwise vorticity in the upper left corner during an upsweep, and positive streamwise vorticity during a corresponding downsweep. In the mean, however, this vorticity is averaged to zero and one is left with the mean streamwise vorticity originating from the inflow duct.

Having access to the POD modes and thus knowledge about the most energetic and largest structures, the r.m.s. value originating from the low-dimensional model of the flow can be computed. This allows us to investigate the origin (e.g. the large or the small scales, respectively) of the contributions to the observed, i.e. total, r.m.s. value. The mean streamwise fluctuations, $(u_{rms}/u_b) \times 100$, given by the first six fluctuating modes are shown in figure 21(*c*,*d*) and compared to the fluctuations from the entire DNS flow field (figure 21*a*,*b*) and the experimental results from Cherry *et al.* (2008) (figure 21*e*,*f*), at two different downstream locations. It can be observed that the

https://doi.org/10.1017/jfm.2012.107 Published online by Cambridge University Press

first six modes (i.e. structures spanning half the length and the entire width of the diffuser) contribute almost entirely to the peaks of the total r.m.s. value. Elsewhere their fluctuations are close to zero. More specifically, by comparing the respective peak values, one can conclude that the r.m.s. values of these large-scale structures contribute 60–80 % to the total r.m.s. peaks. Their contribution increases towards the rear of the diffuser owing to their spatial distribution and will in the last part of the straight section (not shown) constitute more than 90 % of the peaks of the total r.m.s. value. This gives an indication that the bulk of u_{rms} in this region originates from the large-scale oscillation present in the diffuser, rather than from fine-scale turbulence. Note that there is no contradiction here regarding their contribution to the *total* fluctuating energy, since we are only discussing their *local* contribution in a cross-flow plane.

In the DNS and the experimental u_{rms} data in figure 21, one can see the tendency of double peaks. Neither in Cherry *et al.* (2008) nor in Ohlsson *et al.* (2010) was a satisfactory explanation concerning this particular feature provided. However, by considering the fluctuations from the low-dimensional reconstruction, the reason for this can be clarified. First, we note that the u_{rms} from the low-dimensional reconstructed model has even more pronounced double peaks, suggesting that this feature most probably derives from the large-scale motion. To get a better understanding of how this is connected to the movement of the high-speed core of the flow, we will next turn to figure 22. Here, a contour defining 95 % of the maximum streamwise velocity in the low-dimensional reconstructed flow (modes 0–6) is shown (black) for the entire evolution of the flow. Furthermore, the centre of gravity of the area enclosed by the black contour is computed (white). Over the full snapshot time range, this gives rise to a trajectory solely based on the large-scale motion. Consequently, the fluctuations of the peak velocity are greatly reduced as opposed to using the original snapshots, which would be far too chaotic to draw any valuable conclusions. The main directions, as given by this trajectory, are sketched by the white arrows in figure 21(*c*,*d*). By comparing figure 22 with figure 21 we note that the movement of the high-speed core of the flow is located within the area where the minimum of the u_{rms} is found. Around this area, the peaks of u_{rms} are found. At $x = 12$, we observe in figure 22(*a*) that the core moves mainly along the z direction, but with a slight angle to the y axis, in agreement with the r.m.s. minima in figure 21(*a*,*c*,*e*). Further downstream at $x = 20$, in figure 22(*b*), the bulk of the motion goes along the same diagonal as in figure 22(*a*), but with a significant number of excursions in the y direction. The corresponding minimum in the total r.m.s. value is not as distinct an effect as compared to the one at $x = 12$, but is clearly observed in the r.m.s. value pertaining to the low-dimensional model. A plausible explanation for the phenomenon that gives rise to the minimum in u_{rms} and the resulting peaks (two or more) around this minimum is given in figure 23. If we assume that the flapping is entirely in z, a simple model for the flapping jet can be written as

$$u(z, t) = \mathrm{e}^{-[z-\sin(t)]^2}, \quad t \in [0, T], \ \ x \in [-\pi, \pi]. \tag{4.9}$$

The time average and r.m.s. value of this function computed over T are shown in figure 23. We note that the time average has a peak at $z = 0$, i.e. in the interior of the domain, in agreement with the colour map in figure 22. Secondly, we note that the r.m.s. value reaches its minimum where the maximum of the mean is located, i.e. at $z = 0$ in this case. Around this minimum, at the turning points of the jet, the r.m.s. value reaches its highest. This is also what is observed both in the long

https://doi.org/10.1017/jfm.2012.107 Published online by Cambridge University Press

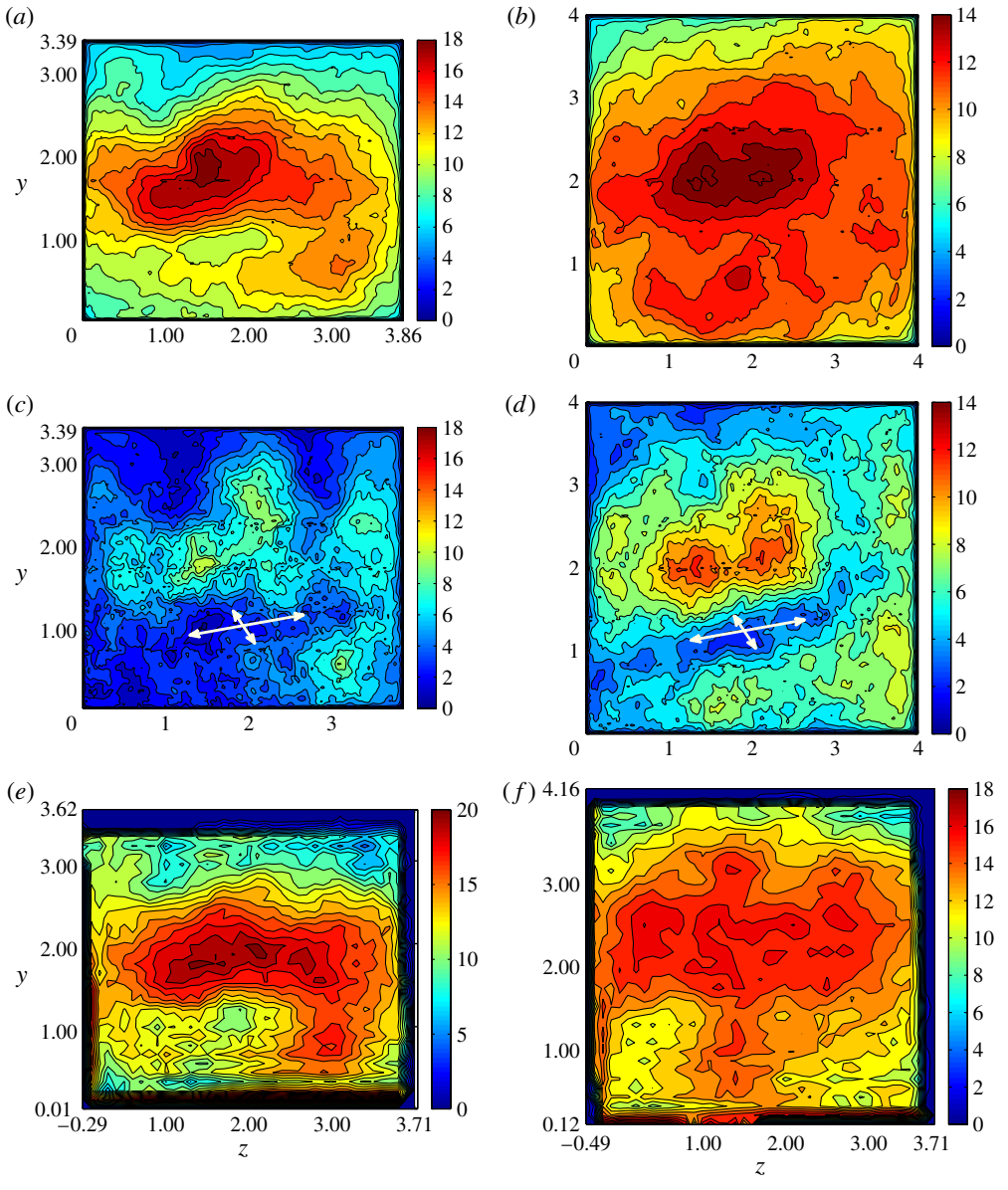


FIGURE 21. Cross-flow planes of streamwise velocity fluctuations, $(u_{rms}/u_b) \times 100$, (*a*,*c*,*e*) $12h$ and (*b*,*d*,*f*) $20h$ downstream of the diffuser throat. (*a*,*b*) Fluctuations from entire flow field. (*c*,*d*) Fluctuations from low-dimensional reconstruction employing the first six fluctuating modes. (*e*,*f*) Experiment by Cherry *et al.* (2008). Contour lines are spaced $200\,u_{rms}/u_b$ apart. White arrows indicate the large-scale movement.

average u_{rms} in figure 21(*a*,*b*), as well as in the experimental data in figure 21(*e*,*f*). In the low-dimensional reconstruction shown in figure 21(*c*,*d*), this effect is strong, with the motion indicated by the white arrows. This is, of course, a simplified model, where we have not taken into account, for example, the deformation of the jet. However, it seems probable that the double peaks and the corresponding minimum found in u_{rms}

https://doi.org/10.1017/jfm.2012.107 Published online by Cambridge University Press

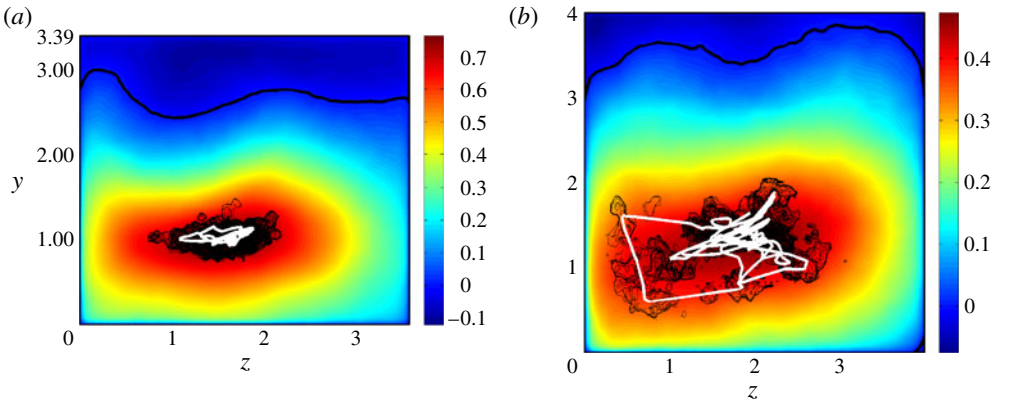


FIGURE 22. Cross-flow planes, (*a*) 12*h* and (*b*) 20*h* downstream of the diffuser throat, coloured by streamwise mean velocity, U/u_b. The thick black line indicates the zero velocity contour. Thin black contours define 95 % of the maximum streamwise velocity of the low-dimensional reconstruction using POD modes 0–6. For each contour, its centre of gravity is shown in white.

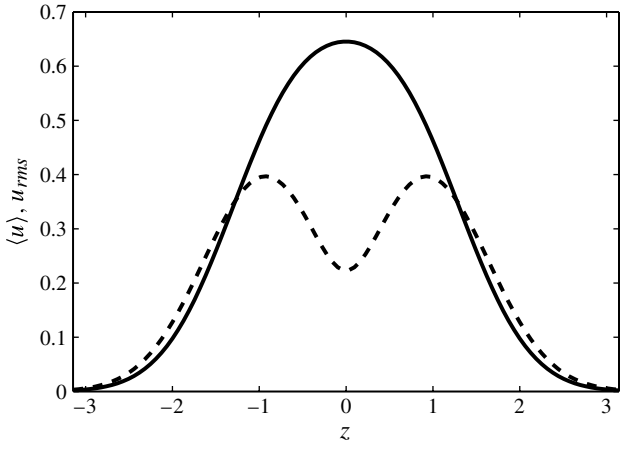


FIGURE 23. Time average (——) and r.m.s. value (– – –) of the function $u(z, t) = \mathrm{e}^{-[z-\sin(t)]^2}$.

are signs of a large-scale motion. It should be pointed out that these conclusions are valid even if only modes 0, 1 and 2 are used for the reconstruction.

5. Conclusions

The flow in a three-dimensional, turbulent and separated diffuser at $Re = 10\,000$ is studied using numerical data from the DNS described in Ohlsson *et al.* (2010), which closely mimics the experiment of 'diffuser 1' by Cherry *et al.* (2008). To this extent, the existing DNS database was extended to account for all possible time scales in the flow. The aim is to elucidate some aspects of the complex physics involved in three-dimensional separation in its own interest, as well as to provide a detailed description

https://doi.org/10.1017/jfm.2012.107 Published online by Cambridge University Press

of this flow, which has recently been established as a test case for turbulence closure models.

We have more rigorously confirmed the findings in Ohlsson *et al.* (2010) that the secondary flow in the inflow duct persists into the diffuser. Owing to the asymmetry of the geometrical set-up, the corner vortices close to the top expanding wall are unequally distributed and diffused, which gives rise to an imbalance of vorticity and causes the separated zone to experience the particular asymmetric behaviour. Using time-resolved information, we could deduce that instantaneous backflow is to a large extent present in the straight section after the diffuser, while the mean flow itself is attached.

Analysis from a set of time signal probes in the flow shows that there is a quasi-periodic motion present in the low-frequency range in a narrow band $St \equiv fh/u_b \in [0.0092, 0.014]$, yielding time periods $T^* = Tu_b/h \in [70, 110]$. The origin of this low frequency is the meandering of the incoming flow, as it interacts with the separated flow in the diffuser. This finding is supported by POD of the flow, where large streamwise streaks spanning half the length and the entire width of the diffuser are identified. In agreement with Moreno *et al.* (2004), this shows that large-scale shedding is present in the flow. Unlike this study, no particular mode could be identified as being dominant in terms of energy. Projections of the flow onto the two-dimensional phase space spanned by the most energetic fluctuating POD modes show evidence that the large scales of the flow behave quasi-periodically, which results in a travelling wave with convection velocity $v_p \approx 0.1$. Owing to the confinement of the flow, this wave creates a strong secondary flow in the cross-flow directions.

The r.m.s. value of the streamwise component, computed from a low-dimensional POD model of the flow, shows that the first few modes contribute 60–80 % to the total u_{rms} peaks in the diffuser, but are close to zero elsewhere. This finding indicates that the bulk u_{rms} in the later part of the diffuser derives from the large-scale oscillation present and provides an explanation for the scattered r.m.s. peaks with a minimum in the centre seen in both the DNS and the experiments. A trajectory of the high-speed core of the flow solely based on a low-dimensional POD model shows that the core of the flow, moves in preferred directions over a relatively long time scale.

Considering the literature on pressure-induced separated flows, most configurations involve at least one homogeneous direction. Diffusers have commonly been studied in two-dimensional configurations, i.e. with a spanwise homogeneous direction. In these flows, no such large-scale spatial coherence, as detected in the present flow case, has to our knowledge been reported. On the other hand, taking into account studies performed on confined jets, low-frequency periodic shedding appears frequently, provided that the walls are close enough to form recirculation zones adjacent to the jet. Owing to the comparably high Reynolds number ($Re = 10\,000$, based on bulk velocity and inflow-duct height) in the present diffuser flow, the momentum of the incoming fluid is high and will, in combination with the large opening angle of the diffuser, consequently share many properties with a turbulent jet bounded by separated flow. We therefore conclude that the reason for the observed large-scale quasi-periodic motion is the confinement in combination with the high Reynolds number and the large separated zone on the top diffuser wall. The dominant frequencies found in the present case coincide remarkably well with the finding by Villermaux & Hopfinger (1994), who identified a low-frequency flapping of $St \sim 0.01$ in the jet. This is also confirmed by Lawson & Davidson (2001), who in a similar set-up reported a very low Strouhal number ($St \ll 1$) when the confinement is such that the jet is bounded by one or two recirculation zones. The observed frequencies in the present flow are likely

https://doi.org/10.1017/jfm.2012.107 Published online by Cambridge University Press

to be the result of a self-sustained oscillation created by a feedback mechanism via the recirculated flow, similar to what was reported by Lawson & Davidson (2001) for the confined jet. To be able to fully confirm this statement, however, more analysis is needed.

Acknowledgements

Computer time was provided by ALCF, Argonne National Laboratory (ANL) on the IBM BG/P (ANL), and by SNIC (Swedish National Infrastructure for Computing) with a generous grant by the Knut and A. Wallenberg (KAW) Foundation at the Centre for Parallel Computers (PDC) at the Royal Institute of Technology (KTH). Dr S. Bagheri is acknowledged for providing a POD code skeleton. We are further grateful to Professor N. Sandham, Dr M. Ilak, O. Semeraro, Dr G. Bellani and Dr O. Tammisola for fruitful discussions.

REFERENCES

ADAMS, N. A. 2000 Direct simulation of the turbulent boundary layer along a compression ramp at $M = 3$ and $Re_\theta = 1685$. *J. Fluid Mech.* **420**, 47–83.

CAZEMIER, W., VERSTAPPEN, R. W. C. P. & VELDMAN, A. E. P. 1998 Proper orthogonal decomposition and low-dimensional models for driven cavity flows. *Phys. Fluids* **10** (7), 1685–1699.

CHERRY, E. M., ELKINS, C. J. & EATON, J. K. 2008 Geometric sensitivity of three-dimensional separated flows. *Intl J. Heat Fluid Flow* **29** (3), 803–811.

CHERRY, E. M., ELKINS, C. J. & EATON, J. K. 2009 Pressure measurements in a three-dimensional separated diffuser. *Intl J. Heat Fluid Flow* **30** (1), 1–2.

DÉLERY, J. M. 2001 Robert Legendre and Henri Werlé: toward the elucidation of three-dimensional separation. *Annu. Rev. Fluid Mech.* **33** (1), 129–154.

EATON, J. K. & JOHNSTON, J. P. 1980 Turbulent flow reattachment – an experimental study of the flow and structure behind a backward-facing step. *Tech. Rep.* MD-39. Thermosciences Division, Stanford University.

FISCHER, P. F. 1997 An overlapping Schwarz method for spectral element solution of the incompressible Navier–Stokes equations. *J. Comput. Phys.* **133** (1), 84–101.

FISCHER, P. F., LOTTES, J. W. & KERKEMEIER, S. G. 2008 nek5000 web page. http://nek5000.mcs.anl.gov.

FRIEDRICH, R. & ARNAL, M. 1990 Analysing turbulent backward-facing step flow with the lowpass-filtered Navier–Stokes equations. *J. Wind Engng. Ind. Aerodyn.* **35**, 101–128.

HERBST, A. H., SCHLATTER, P. & HENNINGSON, D. S. 2007 Simulations of turbulent flow in a plane asymmetric diffuser. *Flow Turbul. Combust.* **79**, 275–306.

HOLMES, P., LUMLEY, J. & BERKOOZ, G. 1996 *Turbulence, Coherent Structures, Dynamical Systems and Symmetry*. Cambridge University Press.

JAKIRLIĆ, S., KADAVELIL, G., KORNHAAS, M., SCHÄFER, M., STERNEL, D. C. & TROPEA, C. 2010*a* Numerical and physical aspects in LES and hybrid LES/RANS of turbulent flow separation in a 3-D diffuser. *Intl J. Heat Fluid Flow* **31** (5), 820–832.

JAKIRLIĆ, S., KADAVELIL, G., SIRBUBALO, E., BREUER, M., VON TERZI, D. & BORELLO, D. 2010*b* In *14th ERCOFTAC SIG15 Workshop on Refined Turbulence Modelling: Turbulent Flow Separation in a 3-D Diffuser*. ERCOFTAC Bulletin, December, Issue 85, case 13.2 (1). ERCOFTAC.

KALTENBACH, H.-J., FATICA, M., MITTAL, R., LUND, T. S. & MOIN, P. 1999 Study of flow in a planar asymmetric diffuser using large-eddy simulation. *J. Fluid Mech.* **390**, 151–185.

KIYA, M. & SASAKI, K. 1985 Structure of large-scale vortices and unsteady reverse flow in the reattaching zone of a turbulent separation bubble. *J. Fluid Mech.* **154**, 463–491.

LANDAHL, M. T. 1980 A note on an algebraic instability of inviscid parallel shear flow. *J. Fluid Mech.* **98**, 243–251.

https://doi.org/10.1017/jfm.2012.107 Published online by Cambridge University Press

LAWSON, N. J. & DAVIDSON, M. R. 2001 Self-sustained oscillation of a submerged jet in a thin rectangular cavity. *J. Fluids Struct.* **15** (1), 59–81.

LE, H., MOIN, P. & KIM, J. 1997 Direct numerical simulation of turbulent flow over a backward-facing step. *J. Fluid Mech.* **330**, 349–374.

LUMLEY, J. L. 1967 The structure of inhomogeneous turbulent flows. In *Atmospheric Turbulence and Radio Wave Propagation* (ed. A. M. Yaglom & V. I. Tatarsky), pp. 166–178. Nauka, Moscow.

LYGREN, M. & ANDERSSON, H. 1999 Influence of boundary conditions on the large scale structures in turbulent plane Couette flow. In *Turbulence and Shear Flow Phenomena 1* (ed. S. Banerjee & J. Eaton), pp. 15–20. Begell House.

MANHART, M. & WENGLE, H. 1993 A spatiotemporal decomposition of a fully inhomogeneous turbulent flow field. *Theor. Comput. Fluid Dyn.* **5**, 223–242.

MAUREL, A., ERN, P., ZIELINSKA, B. J. A. & WESFREID, J. E. 1996 Experimental study of self-sustained oscillations in a confined jet. *Phys. Rev.* E **54** (4), 3643–3651.

MOIN, P. & MOSER, R. 1989 Characteristic-eddy decomposition of turbulence in a channel. *J. Fluid Mech.* **200**, 471–509.

MORENO, D., KROTHAPALLI, A., ALKISLAR, M. B. & LOURENCO, L. M. 2004 Low-dimensional model of a supersonic rectangular jet. *Phys. Rev.* E **69** (2), 026304.

NA, Y. & MOIN, P. 1998 Direct numerical simulation of a separated turbulent boundary layer. *J. Fluid Mech.* **374**, 379–405.

OHLSSON, J., SCHLATTER, P., FISCHER, P. F. & HENNINGSON, D. S. 2010 Direct numerical simulation of separated flow in a three-dimensional diffuser. *J. Fluid Mech.* **650**, 307–318 (note change of name from J. Ohlsson to J. Malm).

PIQUET, J. 1999 *Turbulent Flows: Models and Physics*. Springer.

ROWLEY, C. W., MEZIĆ, I, BAGHERI, S, SCHLATTER, P & HENNINGSON, D. S. 2009 Spectral analysis of nonlinear flows. *J. Fluid Mech.* **641**, 115–127.

SCHLATTER, P., ÖRLÜ, R., LI, Q., BRETHOUWER, G., FRANSSON, J. H. M., JOHANSSON, A. V., ALFREDSSON, P. H. & HENNINGSON, D. S. 2009 Turbulent boundary layers up to $Re_\theta = 2500$ studied through numerical simulation and experiments. *Phys. Fluids* **21** (5), 051702.

SCHNEIDER, H., VON TERZI, D. A., BAUER, H. J. & RODI, W. 2010 Reliable and accurate prediction of three-dimensional separation in asymmetric diffusers using large-eddy simulation. *J. Fluids Engng* **132**, 031101.

SIMPSON, R. L. 1981 A review of some phenomena in turbulent flow separation. *Trans. ASME: J. Fluids Engng* **102**, 520–533.

SIMPSON, R. L. 1989 Turbulent boundary-layer separation. *Annu. Rev. Fluid Mech.* **21** (1), 205–232.

SIROVICH, L. 1987 Turbulence and the dynamics of coherent structures. Parts I–III. *Q. Appl. Maths* **45**, 561–590.

SPILLE-KOHOFF, A. & KALTENBACH, H.-J. 2001 Generation of turbulent inflow data with a prescribed shear-stress profile. In *DNS/LES Progress and Challenges, Third AFSOR Conference on DNS and LES, Arlington, Texas* (ed. C. Liu, L. Sakell & T. Beutner). Greyden Press.

TÖRNBLOM, O., LINDGREN, B. & JOHANSSON, A. V. 2009 The separating flow in a plane asymmetric diffuser with 8.5° opening angle: mean flow and turbulence statistics, temporal behaviour and flow structures. *J. Fluid Mech.* **636**, 337–370.

TUFO, H. M. & FISCHER, P. F. 2001 Fast parallel direct solvers for coarse grid problems. *J. Parallel Distrib. Comput.* **61** (2), 151–177.

VILLERMAUX, E. & HOPFINGER, E. J. 1994 Self-sustained oscillations of a confined jet: a case study for the nonlinear delayed saturation model. *Physica* D **72** (3), 230–243.

WANG, C., JANG, Y. J. & LESCHZINER, M. A. 2004 Modelling two- and three-dimensional separation from curved surfaces with anisotropy-resolving turbulence closures. *Intl J. Heat Fluid Flow* **25** (3), 499–512.

https://doi.org/10.1017/jfm.2012.107 Published online by Cambridge University Press